

JGR Oceans

RESEARCH ARTICLE

10.1029/2024JC021204

Key Points:

- The submesoscale salinity (temperature) fronts are pronounced at surface (subsurface), and they tend to be compensated
- Subsurface layer is featured with more compensation than surface layer, and this subsurface compensation is more submesoscale-selective
- The slump of salinity-controlled compensated fronts leads to temperature inversion and the retention of barrier layer

Supporting Information:

Supporting Information may be found in the online version of this article.

Correspondence to:

X. Cheng,
xuhuacheng@hhu.edu.cn

Citation:

Duan, W., Cheng, X., Zhou, Y., & Gula, J. (2024). Characteristics of submesoscale compensated/reinforced fronts in the northern Bay of Bengal. *Journal of Geophysical Research: Oceans*, 129, e2024JC021204. <https://doi.org/10.1029/2024JC021204>

Received 11 APR 2024

Accepted 11 SEP 2024

Author Contributions:

Conceptualization: Xuhua Cheng
Formal analysis: Yifei Zhou
Funding acquisition: Xuhua Cheng
Methodology: Wei Duan
Supervision: Xuhua Cheng, Jonathan Gula
Writing – original draft: Wei Duan
Writing – review & editing: Xuhua Cheng, Yifei Zhou, Jonathan Gula

Characteristics of Submesoscale Compensated/Reinforced Fronts in the Northern Bay of Bengal

Wei Duan^{1,2}, Xuhua Cheng¹ , Yifei Zhou¹, and Jonathan Gula^{2,3} 

¹College of Oceanography, Hohai University, Nanjing, China, ²Laboratoire d'Océanographie Physique et Spatiale (LOPS), University Brest, CNRS, IRD, Ifremer, INRIA, IUEM, Brest, France, ³Institut Universitaire de France (IUF), Paris, France

Abstract Fronts in the Bay of Bengal (BoB) are active and can potentially impact the regional dynamics such as temperature variability, salinity distribution and oceanic circulation. Based on the high resolution model output (LLC4320), this study investigates the characteristics of submesoscale fronts in the northern BoB and associated compensation/reinforcement effects. At sea surface, horizontal gradients of salinity and density are remarkable in the northern BoB, and they are nearly 3 times larger than temperature gradients. As the depth deepens, temperature gradients increase and become comparable to salinity gradients, while density gradients decrease a lot due to the increasing effects of compensation at subsurface. Statistical results show the dominance of salinity-controlled fronts over temperature-controlled fronts, and compensated fronts over reinforced fronts. The surface cooling/heating results in significant temporal variation of compensation at surface, but this variation is limited at subsurface by the blocking of the mixed layer base. The submesoscale-selective feature of compensation is much more pronounced at subsurface layer than surface layer. From statistical analysis and idealized numerical model, we found the slump of salinity-controlled compensated fronts are important in generating temperature inversion and maintaining barrier layer. This study validates the compensation theories originating from observations, and further illustrates the importance of subsurface compensated fronts using spatially continuous, regionally extended and longer-term model output. The subsurface-intensified submesoscale-selective compensation is proved for the first time in this study.

Plain Language Summary With cold, fresh water on the one side and warm, salty water on the other side, roles of temperature and salinity in changing density are opposed across fronts, and they are referred to as compensated fronts. Otherwise, the fronts are reinforced by temperature and salinity. The strength of compensated fronts are thwarted to some extent compared to reinforced fronts, thus the existence of compensation effects are not favorable for forming a sharp front and associated instability processes. The statistics of submesoscale compensated/reinforced fronts in the northern BoB are comprehensively analyzed in this study. Concerning the amount of freshwater input, fronts are dominated by salinity gradients instead of temperature gradients over the northern BoB, and compensated fronts are more likely to form during winter with the existence of both large salinity gradients and heat losses. Both statistical analysis and idealized model simulation suggest that when the salinity front compensated by temperature collapses, a reversed vertical temperature gradient (temperature inversion) is favored to form.

1. Introduction

The Bay of Bengal (BoB) is a semi-enclosed basin in the northeastern Indian Ocean. The thermohaline structure in the BoB is very unique among the world's ocean basins. A freshwater plume exists in the northern Bay of Bengal (nBoB) due to freshwater input from oceanic monsoon precipitation and associated continental river discharge (Papa et al., 2012; Sengupta et al., 2006; Varkey et al., 1996). Freshwater input creates a strong salinity stratification in the upper ocean of the nBoB, forming barrier layers (where halocline deeper than thermocline) and temperature inversion layers (where warm water between colder water above and below) in this region (Lukas & Lindstrom, 1991; Sprintall & Tomczak, 1992; Thadathil et al., 2002). Temperature inversion layer and barrier layer usually coexist, and they are crucial in modulating local air-sea momentum and heat exchange, and thus impacting climate and post-monsoon tropical cyclones (Thadathil et al., 2016).

Fronts are ubiquitous in the ocean and are characterized by sharp horizontal variations in temperature, salinity, density or other material concentrations, with horizontal scales ranging from meters to kilometers (McWilliams, 2021). For example, the Kuroshio, Gulf Stream, and Antarctic Circumpolar Current are known for their

prominent horizontal temperature gradients across their major axes (Clayton et al., 2014; Wenegrat et al., 2020; Wunsch, 1998) and they are largely constrained by Earth's rotation.

Submesoscale fronts with horizontal scales of $0.1 \sim 10$ km and time scales of hours \sim days are widely distributed over the global ocean (McWilliams, 2016). These fronts are associated with relatively larger Rossby numbers ($O \sim (1)$) and are thus less constrained by the geostrophic effect (Thomas et al., 2008). The generation mechanisms of submesoscale fronts and filaments (considered as dual fronts) are illustrated by previous researchers: strain-induced frontogenesis (Hoskins & Bretherton, 1972), mixed layer instability (Boccaletti et al., 2007), horizontal convergence motion (Barkan et al., 2019) and boundary layer turbulence (McWilliams et al., 2015). Vertical velocities around submesoscale fronts are typically large due to the development of ageostrophic secondary circulation, making them instrumental in influencing oceanic biogeochemical processes (Lévy et al., 2018; Mahadevan, 2016) and marine pollutant distributions (Poje et al., 2014). Besides, submesoscale fronts provide a connection between mesoscale and small scale processes for energy cascade (Arbic et al., 2022; Balwada et al., 2022; Barkan et al., 2021; Garabato et al., 2022; Yu et al., 2021).

Although the small spatiotemporal scale of submesoscale fronts makes them difficult to resolve observationally, several studies have observed submesoscale fronts in the BoB using advanced observational means. For example, Sengupta et al. (2016) observed high-frequency salinity variations in the nBoB based on a long time series of mooring observations. They suggested that a salinity jump with magnitude of 0.2–1.2 PSU occurs when submesoscale salinity fronts moving pass the mooring. Based on a high-resolution radiator survey in the central BoB from the Air–Sea Interactions in the Northern Indian Ocean (ASIRI)—Ocean Mixing and Monsoons (OMM) project (Wijesekera et al., 2016), abundant submesoscale temperature and salinity fronts were observed by Ramachandran et al. (2018). They believed that these submesoscale fronts are important in modulating the ocean vertical stratification. More recently, using the Monsoon Intraseasonal Oscillations in the Bay of Bengal (MISO-BOB) observations, Mckie et al. (2024) suggested that the submesoscale frontal instability and temperature inversion are closely related in the BoB.

High-resolution numerical modeling is a powerful tool for studying submesoscale fronts. Based on outputs from a high-resolution air-ocean-wave coupled model, Jensen et al. (2018) found that the submesoscale salinity front can evolve into submesoscale currents in the mixed layer through frontal instabilities. Using Large Eddy Simulation (LES) results, Sarkar et al. (2016) suggested that the submesoscale salinity fronts in the nBoB are associated with a variety of instability processes (e.g., symmetric instability and Kelvin-Helmholtz shear instability), and further development of the instability processes can alter the ocean stratification. Based on LES, Pham and Sarkar (2019) found that strong salinity fronts are prone to shear instability, which drives the generation of ageostrophic secondary circulations, leading to the formation of barrier layers and temperature inversion layers on both sides of the front, and enhancing local mixing.

Compensating/opposing (these two terms are used interchangeably in this study) effects are common across oceanic fronts when the roles of salinity and temperature in density variation are opposite (i.e., warm/salty water on one side and cold/fresh water on the other side) (Rudnick & Martin, 2002). Density fronts at $\sim O(10$ km) scales tend to be compensated in many regions (Drushka et al., 2019), and the universality of the compensation in the North Pacific Ocean (Rudnick & Ferrari, 1999) and the Gulf of Mexico (Barkan et al., 2017) has been captured by cruise observations and model simulations, respectively. Lin et al. (2023) used towed measurements to reveal the mechanism of scale-dependent compensation in the Taiwan Strait. They suggested that the compensation effects at submesoscale are larger (smaller) in salinity (temperature) dominated frontal zones compared to larger scales. In the BoB, Spiro Jaeger and Mahadevan (2018) investigated the temperature-salinity compensation effect across fronts using ship-based observations and model simulations. They proposed that the restratification effect resulting from submesoscale frontal instability could transform lateral gradients into mixed-layer stratification. Consequently, when cooled by the atmosphere, the sea surface temperature (SST) decreases more significantly on the restratified side of the salinity-controlled front owing to the shallower mixed layer. This leads to the occurrence of temperature-salinity compensation.

The above-mentioned studies of submesoscale fronts are based on either observations or idealized numerical models. However, the spatial coverage (both horizontal and vertical) and the time span of the observations are

Table 1
Observations and Reanalysis Data Used in This Study

Data	Temporal resolution	Spatial resolution	Variable(s)
SMOS	7 Days	0.25° × 0.25°	SSS
GHRSST	Daily	0.01° × 0.01°	SST
MODIS	Daily	4 km	SST
WOA18	Monthly	0.25° × 0.25°	Salinity, temperature

limited, and idealized models are limited to describe the real oceanic fronts. Besides, a general conclusion on temperature-salinity compensation or reinforcement across fronts is still lacking. In this study, a comprehensive analysis of submesoscale fronts and the associated compensation/reinforcement effects is performed in the BoB using a spatially continuous, regionally extended, and longer-term model output.

The remainder of the manuscript is structured as follows: Data and methods are described in Section 2. Model outputs are validated in Section 3. Statistics of submesoscale fronts in the BoB are presented in Section 4. Compensation and reinforcement effects across submesoscale fronts are illustrated in Section 5. The relationship between compensated fronts and vertical stratification is shown in Section 6. Discussion and conclusions are given in Section 7.

2. Data and Method

2.1. Numerical Model Output

A high resolution primitive equation model is used to provide high resolution thermohaline data in the BoB (3°N–23°N, 76°E–99°E). This model is the Massachusetts Institute of Technology General Circulation Model (MITgcm) on a latitude-longitude polar cap (LLC) grid (Menemenlis et al., 2008) for a period of 14 months from 13 September 2011 to 14 November 2012. The model simulation used here is the so-called LLC4320, which has a horizontal grid spacing of 1/48° (~2 km in the BoB). The vertical resolution of this model is refined at surface layer: grid space increases from 1 m at surface to 380 m at bottom, with 22 layers in the upper 100 m. The temporal resolution of the model output is 1 hour, and the daily averaged data are selected for analysis in order to remove the tidal signals.

The model is forced with six-hourly surface atmospheric fields (including momentum and buoyancy flux) from the European Center for Medium-Range Weather Forecasting (ECMWF) atmospheric operational model analysis (with a horizontal resolution of 0.14°). The climatological river discharge over the BoB is included in the surface freshwater flux. Full luni-solar tidal constituents are also included in this simulation as additional atmospheric pressure forcing. The vertical subgrid mixing scheme used in the model is the K-Profile Parameterization (KPP). This model output has been successfully used in submesoscale studies (e.g., Cheng et al., 2023; Dong et al., 2021; Rocha et al., 2016; Su et al., 2018; Zhou et al., 2024). In this study, a period of one full year (1 October 2011 ~ 30 September 2012) is chosen for the analysis.

2.2. Multisource Data

We use several observational data sets to validate the numerical model. Sea surface salinity (SSS) and temperature (SST) data with a 7-day interval are obtained from Soil Moisture and Ocean Salinity SMOS/SMAP OI L4 maps product (SMOS for short) provided and supported by the CNES CATDS and CNES TOSCA SMOS OCEAN projects (Kolodziejczyk et al., 2021). Daily SST data are from the Group of High-Resolution Sea Surface Temperature (GHRSST) product with a 0.01° × 0.01° resolution (Dash et al., 2012). We also use SST data from Aqua Moderate Resolution Imaging Spectroradiometer (MODIS, Savtchenko et al., 2004) with a resolution of 4 km. The World Ocean Atlas 2018 (WOA18) provides vertical thermohaline data (Locarnini et al., 2018; Zweng et al., 2018). The time period for all data is from October 2011 to September 2012, except that WOA18 is monthly climatology. Detailed information about these data can be found in Table 1.

2.3. Idealized Numerical Model

The Coastal and Regional Ocean CCommunity model (CROCO, Auclair et al., 2022), is used to set up frontal experiments to corroborate the findings from statistical analysis (see Section 6 for detail). The fronts we set are in a channel measuring 60 km (along front) × 60 km (cross front) and 25 m (vertically), with a horizontal resolution of 2 km and a vertical resolution of 1 m. The frontal axes are along the y-direction with a hyperbolic function

Table 2
Parameter Setups for Different Fronts

Parameter	TCSR	SCTR	SCTO	TCSO
$\nabla S_x _{max}$	$1 \times 10^{-6} s^{-2}$	$6 \times 10^{-6} s^{-2}$	$6 \times 10^{-6} s^{-2}$	$1 \times 10^{-6} s^{-2}$
S_0	-230	-39	-39	-230
Sgn	1	1	-1	-1

along the x -direction. Temperature and salinity across the fronts are set to be similar with that of Pham and Sarkar (2019) by:

$$T(x, z) = \frac{\nabla T_x|_{max} L}{60\alpha g} \left\{ T_0 + 0.25 \left[1 + \tan h \left(x - \frac{L}{2} \right) \frac{12}{L} \right] \left[1 + \tan h \left(\frac{z+H}{2} \right) \right] \right\} \\ - \frac{0.5}{\alpha g} \left\{ [N_{m,T}^2 + N_{p,T}^2] z + 2(N_{m,T}^2 - N_{p,T}^2) \log \left[\frac{\cos h((z+H)/2)}{\cos h(H/2)} \right] \right\} \quad (1)$$

$$S(x, z) = \frac{-\nabla S_x|_{max} L}{60\beta g} \left\{ S_0 + 0.25 \left[1 + Sgn * \tan h \left(x - \frac{L}{2} \right) \frac{12}{L} \right] \left[1 + \tan h \left(\frac{z+H}{2} \right) \right] \right\} \\ - \frac{0.5}{\beta g} \left\{ [N_{m,S}^2 + N_{p,S}^2] z + 2(N_{m,S}^2 - N_{p,S}^2) \log \left[\frac{\cos h((z+H)/2)}{\cos h(H/2)} \right] \right\} \quad (2)$$

where $\nabla T_x|_{max} = 2 \times 10^{-6} s^{-2}$ is the maximum values of the lateral gradients of temperature; $L = 60$ km is the frontal width; $\alpha = 2 \times 10^{-4} \text{ }^\circ\text{C}^{-1}$ is the thermal expansion coefficient and $\beta = 8 \times 10^{-4} \text{ PSU}^{-1}$ is the haline contraction coefficient; $T_0 = 26$ is a parameter to make the temperature close to reality; $N_{m,T}^2 = -2 \times 10^{-5} s^{-2}$ and $N_{p,T}^2 = -2 \times 10^{-4} s^{-2}$ are the temperature stratification in the mixed layer and the pycnocline, respectively; $N_{m,S}^2 = 4 \times 10^{-4} s^{-2}$ and $N_{p,S}^2 = 2 \times 10^{-3} s^{-2}$ are the salinity stratification in the mixed layer and pycnocline, respectively. These values are set to constant, so that the temperature structures are the same for all fronts (see first column in Figure 13).

On the other hand, we change the following parameters according to the values of the Turner angle (see Section 5 for detailed definition): (a) the maximum values of the lateral gradients of salinity ($\nabla S_x|_{max}$); (b) parameter to adjust the salinity close to reality (S_0); and (c) a sign function (Sgn). This results in different salinity structures for different fronts (see second column in Figure 13). The values of these parameters are listed in Table 2, and the way to classify a front (TCSR, SCTR, SCTO and TCSO) is described in Section 5.

3. Model Validation

3.1. Surface Temperature/Salinity

We first validate the ability of LLC4320 to simulate oceanic properties in the BoB. Although there are small discrepancies, the seasonal cycles of SSS and SST in LLC4320 agree quite well with the observed SSS (from SMOS) and SST (from GHRSST) (Figure 1). The spatio-temporal distribution of hydrological properties in the BoB is well represented in this simulation. The largest variations in SST/SSS are located in the northern bay (boxes in Figures 1, 16°N–22.5°N, 83°E–95°E, hereafter region R1), partly due to the large inputs and/or variations of heat/freshwater fluxes in this region (Figure S1 in Supporting Information S1).

3.2. Vertical Thermohaline

The vertical thermohaline distribution of the model is also evaluated through comparing it with observation. We focus on region R1, which is subject to the largest SSS/SST variability (Figure S1 in Supporting Information S1). The model is shown to reproduce the seasonal cycles of the subsurface thermohaline distribution well by comparing with the WOA18 monthly climatology data (Figures 2a–2d). In particular, both model and observation capture the strong surface layer cooling in winter and warming in spring/summer (Figure 2e). In addition, the upper ocean freshening event due to the increasing freshwater flux in late summer and autumn (Figure 2f) is well captured by the model and observation.

The barrier layer is well known in the ocean, especially in the BoB, for its climatic effect, and the barrier layer thickness (BLT) is a good indicator to describe the ocean salinity stratification. The BLT is calculated based on the variable density threshold method following De Boyer Montegut et al. (2004): First, we define a reference depth ($Z_{ref} = 0$ m) and find the depth at which the temperature decreases by 0.5°C compared to the temperature at Z_{ref} , which gives us the isothermal layer depth (ILD). Then we calculate the density variation from Z_{ref} with a constant salinity and a 0.5°C temperature decrease ($\delta\rho$). Finally, we search for the depth at which the density

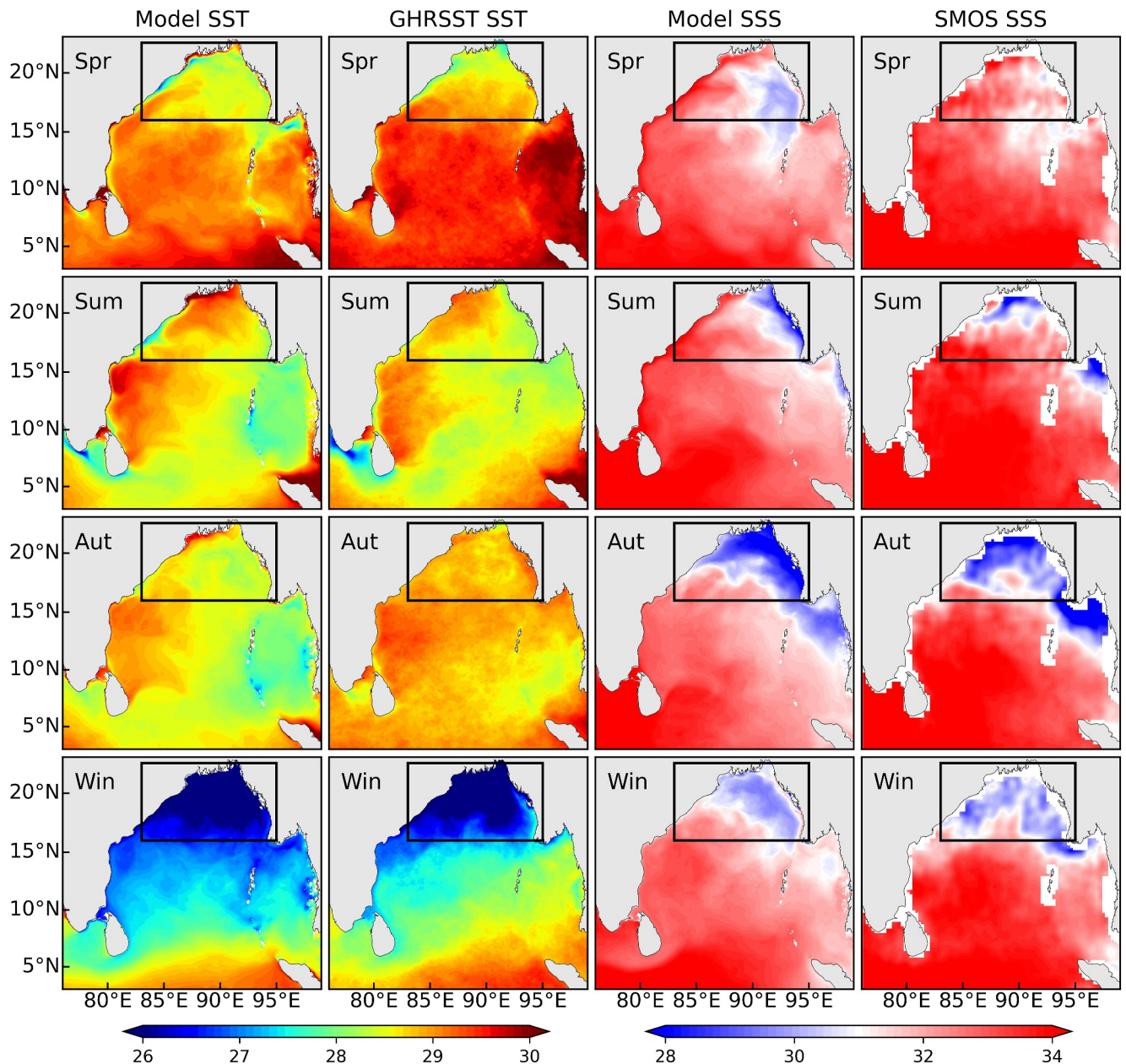


Figure 1. Geographical distribution of model seasonal SST (first column, °C), GHRSST seasonal SST (second column, °C), model seasonal SSS (third column, PSU), and SMOS seasonal SSS (last column, PSU) during October 2011–September 2012. Black boxes refer to region R1.

increase from Z_{ref} is equal to $\delta\rho$, and this depth is defined as the mixed layer depth (MLD). The layer thickness between the MLD and the ILD is defined as the BLT.

The BLT corresponds to the layer between the black line (MLD) and the blue line (ILD) in Figures 2a–2d. The seasonal variation of the BLT in the model agrees well with the WOA18 data, with a maximum in winter and a minimum in spring. During winter, when the barrier layer is thickest and heat exchange between the surface and subsurface layers is blocked, both WOA18 and LLC4320 capture a subsurface temperature inversion at a depth of 40–60 m. These validations confirm the robust thermohaline representation of the model and provide substantial credibility for conducting further analysis.

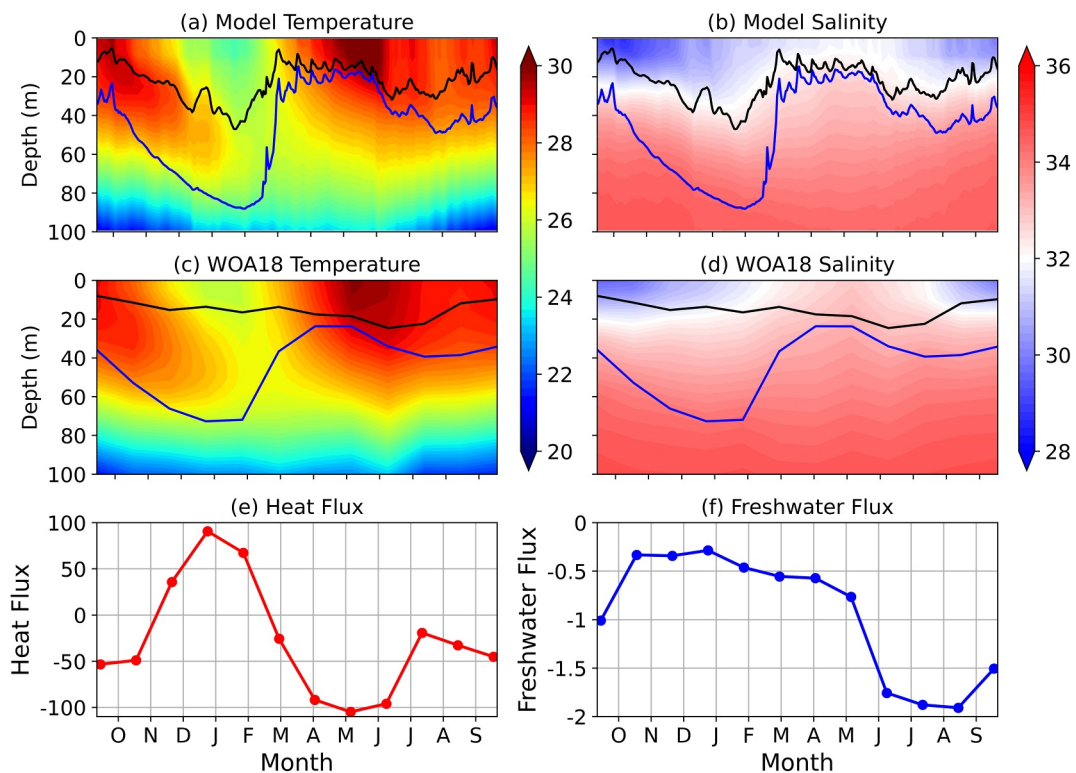


Figure 2. Depth-time plot of (a) temperature ($^{\circ}\text{C}$) and (b) salinity (PSU) averaged over region R1 based on LLC4320 during October 2011–September 2012. (c and d) Are the thermohaline structure from WOA18 monthly climatology data. (e) Regional mean heat flux in the model (upward, positive value means surface cooling, W/m^2). (f) Regional mean freshwater flux in the model (upward, positive value means losing freshwater, cm/day). Black lines in (a–d) represent the MLD and blue lines in (a–d) represent the ILD. The layer in between is the barrier layer.

3.3. Typical Length of Submesoscale

Based on the theory of baroclinic instability (Boccaletti et al., 2007; Dong et al., 2020), the upper bound of the mixed layer baroclinic instability wavelength is $L = 6 \frac{N_{ML} H_{ML}}{f}$, where N_{ML} is the mixed layer stratification, H_{ML} is the mixed layer depth, and f is the Coriolis parameter. The values of L in the study area are within the range of $15 \sim 50$ km (Figure 3), so the submesoscale fronts can be at least partially resolved by LLC4320 with its grid resolution of O (~ 2 km). The regional mean L over the nBoB is about 28 km, so hereafter the submesoscale fronts are defined as fronts with scales $\sim O$ (10–30 km).

4. Statistics of Submesoscale Fronts in the BoB

4.1. Observed Submesoscale Fronts

Ocean fronts are characterized by large horizontal gradients of tracers. A snapshot of SST from MODIS (Figure 4a) on a typical winter day shows amounts of temperature fronts in the Bay of Bengal with horizontal scales of $\sim O$ (1) km, which can be considered as submesoscale fronts (Li et al., 2022; Sengupta et al., 2016). These submesoscale fronts are also obvious in LLC4320 (Figure 4b).

4.2. Lateral Gradients for Tracers

To represent the frontal characteristics in the BoB, the zonal and meridional gradients of temperature, salinity and density scaled by their respective coefficients are calculated as:

$$\nabla T_x = -g\alpha\partial T/\partial x; \nabla T_y = -g\alpha\partial T/\partial y \quad (3.1)$$

$$\nabla S_x = g\beta\partial S/\partial x; \nabla S_y = g\beta\partial S/\partial y \quad (3.2)$$

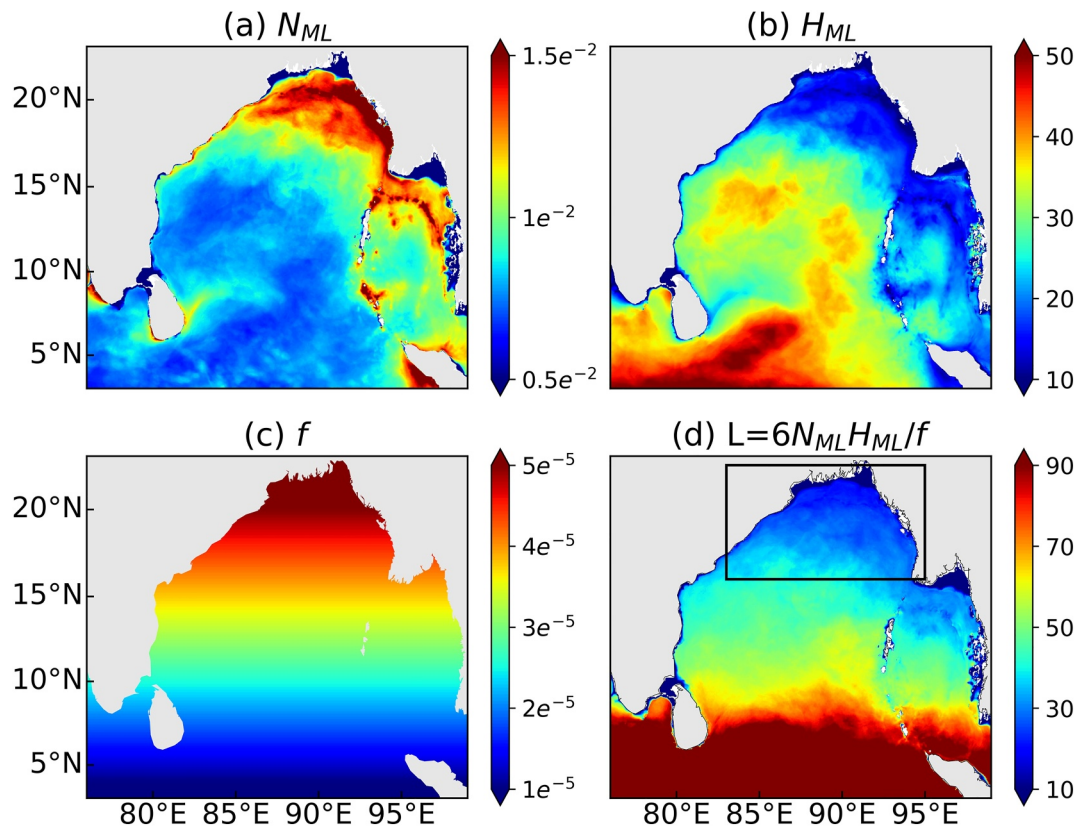


Figure 3. Spatial distribution of annual mean (a) mixed layer stratification (s^{-1}), (b) mixed layer depth (m), (c) Coriolis parameter (s^{-1}) and (d) upper bound of mixed layer baroclinic instability wavelength (km). Black box in (d) refers to region R1.

$$\nabla\rho_x = \nabla T_x + \nabla S_x; \quad \nabla\rho_y = \nabla T_y + \nabla S_y \quad (3.3)$$

where T , S and ρ are temperature, salinity and density, respectively. α is the thermal expansion coefficient and β is the haline contraction coefficient. x and y are the zonal and meridional direction, respectively. These scaled gradients are adjusted to have the same unit (s^{-2}), facilitating easier comparison. Hereafter we will simply refer to the “scaled gradients” of temperature, salinity, and density as “gradients.”

Spice (γ) is a passive tracer that combines the gradients of temperature and salinity on isopycnal surfaces (Spiro Jaeger et al., 2020). BoB region is a typical “spicy sea” suggested by MacKinnon et al. (2016), which represents a region in which there is significant temperature salinity (T-S) variability along an isopycnal. The scaled spice gradients are calculated as:

$$\nabla\gamma_x = \nabla S_x - \nabla T_x; \quad \nabla\gamma_y = \nabla S_y - \nabla T_y \quad (3.4)$$

The results that will be discussed below are based on the zonal (x direction) gradients, while the results based on meridional (y direction) gradients are shown in Supporting Information S1 for comparison. It can be seen that most of the results are statistically independent of direction. Hereafter we use “gradients” as a shortening for “scaled zonal gradients.”

The annual mean amplitude of gradients at the sea surface for temperature, salinity, and density in the BoB are shown in Figures 5a–5c. Spatially, the largest gradients of salinity and density are visible in region R1 (black boxes). This region receives large amounts of freshwater from precipitation and river runoff (Figure S1 in Supporting Information S1), and large gradients are formed by the stirring of ocean currents. Large salinity and density gradients are also visible in the coastal regions (i.e., east coast of India, coast of Sri Lanka, west coast of

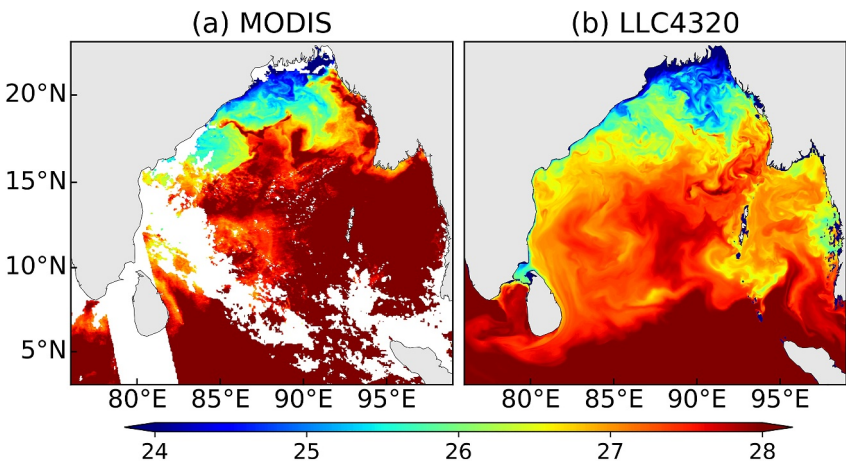


Figure 4. Snapshots of SST ($^{\circ}$ C) on 31 December 2011 from (a) MODIS and (b) LLC4320 over the BoB region. Missing data in (a) are cloud covered regions.

Myanmar, Andaman Islands, and southern part of Sumatra). These regions have very shallow water depths (shoreward of the 200 m isobaths in Figure 5), so the ocean-land interaction can induce large gradients. The surface temperature gradients are much smaller compared to that of salinity and density (Figure 5a). From Equation 3.3, the horizontal density gradients are exactly the sum of the temperature gradients and the salinity gradients, so that at sea surface most of the density gradients are caused by salinity rather than temperature. This

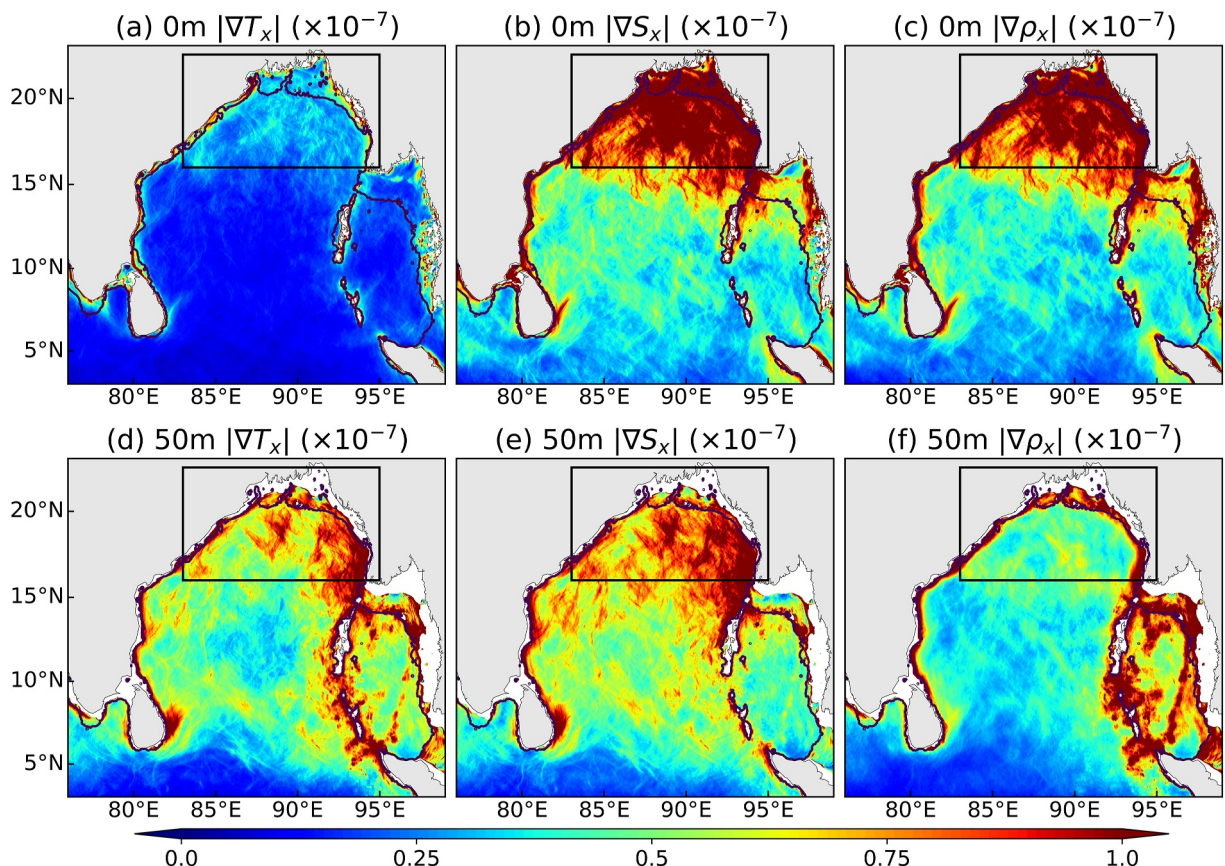


Figure 5. Spatial distribution of annual mean (October 2011–September 2012) sea surface (0 m) (a) $|\nabla T_x|$, (b) $|\nabla S_x|$ and (c) $|\nabla \rho_x|$ in the BoB, multiplied by 10^{-7} (d–f) are subsurface (50 m) values. Units are s^{-2} . The black boxes refer to region R1 and the black contours indicate the 200 m isobaths from ETOPO2.

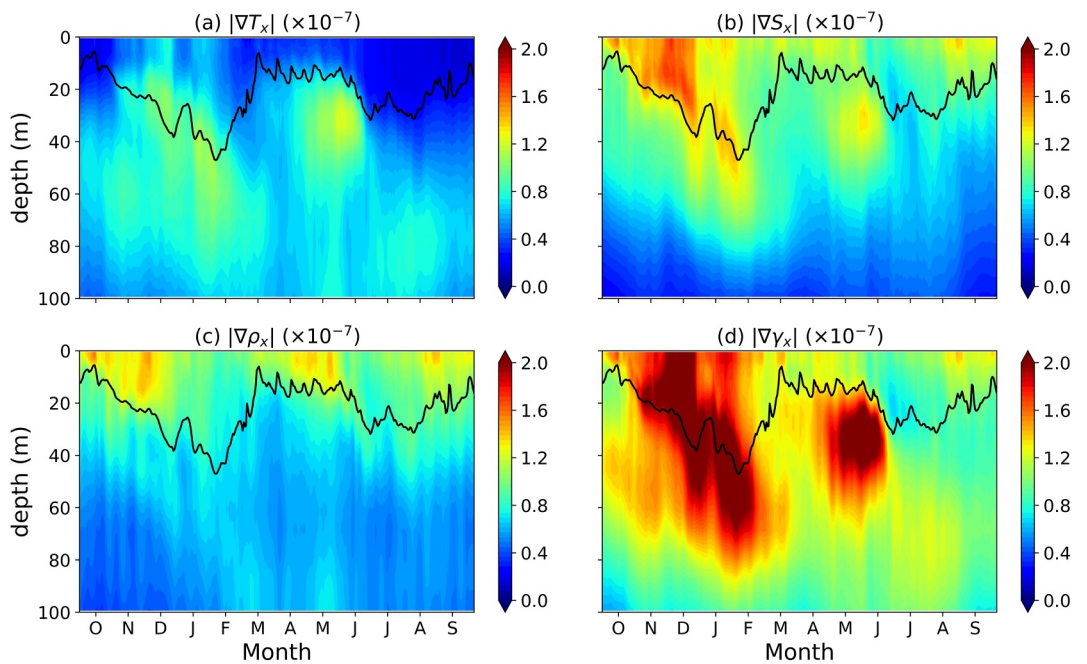


Figure 6. Depth-time plot of lateral averaged (a) $|\nabla T_x|$, (b) $|\nabla S_x|$, (c) $|\nabla \rho_x|$ and (d) $|\nabla \gamma_x|$ during October 2011 and September 2012 over region R1. The black lines in each panel show the mixed layer depth.

salinity-controlled feature is also obvious in the surface temperature-salinity diagram (Figure S2a in Supporting Information S1).

The gradients at subsurface are quite different from those at surface. Here the depth for subsurface is chosen as 50 m, that is, the depth just below the mixed layer depth (Figure 2). The values of $|\nabla T_x|$ in the subsurface are much larger than those at surface (Figure 5d), while $|\nabla S_x|$ and $|\nabla \rho_x|$ are smaller than those at surface (Figures 5e and 5f). In particular, $|\nabla \rho_x|$ in the subsurface is much smaller than $|\nabla S_x|$ and $|\nabla T_x|$, and large values of $|\nabla \rho_x|$ are mostly confined to the coastal regions. In other words, most of the $|\nabla T_x|$ and $|\nabla S_x|$ are opposed in the subsurface, producing small $|\nabla \rho_x|$. Compared to the surface, the salinity-controlled features are much reduced in the subsurface (see also Figure S2b in Supporting Information S1). Note that over the southeastern BoB region, subsurface gradients of temperature and density are also remarkable. This region is featured with relative shallow water depth, so the topography may be crucial in generating large gradients. However, this is beyond the scope of the current study and will be addressed in future research.

Obviously, large tracer gradients are not just confined to the surface layer. The depth-time plots for laterally averaged $|\nabla T_x|$, $|\nabla S_x|$, $|\nabla \rho_x|$ and $|\nabla \gamma_x|$ over region R1 are shown in Figure 6 in order to get a vertical view. Values of $|\nabla T_x|$ are relatively small in the mixed layer and reach a maximum below the MLD (Figure 6a), which may be related to the intermittent tilting of the isotherms. In contrast, large $|\nabla S_x|$ are mostly confined to the mixed layer and decrease with depth (Figure 6b). The density gradients are mostly smaller than the salinity gradients, indicating that the effects of temperature and salinity on the density gradients are counteracted. On the contrary, the value of $|\nabla \gamma_x|$ is larger than all other tracer gradients, suggesting a large variation of thermohaline properties along isopycnals. Clearly, $|\nabla \gamma_x|$ acts in the opposite direction to $|\nabla \rho_x|$, and large magnitudes of $|\nabla \gamma_x|$ can be considered as a sign of temperature-salinity compensation.

4.3. Selection of Submesoscale Fronts

Since fronts are characterized by particularly large gradients, strong submesoscale frontal regions are defined here as locations with remarkable horizontal gradients. The probability density function (PDF) for $|\nabla T_x|$, $|\nabla S_x|$ and $|\nabla \rho_x|$ at surface and subsurface are shown in Figure 7 (solid lines). The dashed lines represent the largest 5% (8% or 10% doesn't make large differences, not shown) magnitude for each gradient, where the PDF slopes flatten (Barkan et al., 2017; Lin et al., 2023; Spiro Jaeger & Mahadevan, 2018). At the surface (blue lines in Figure 7), the

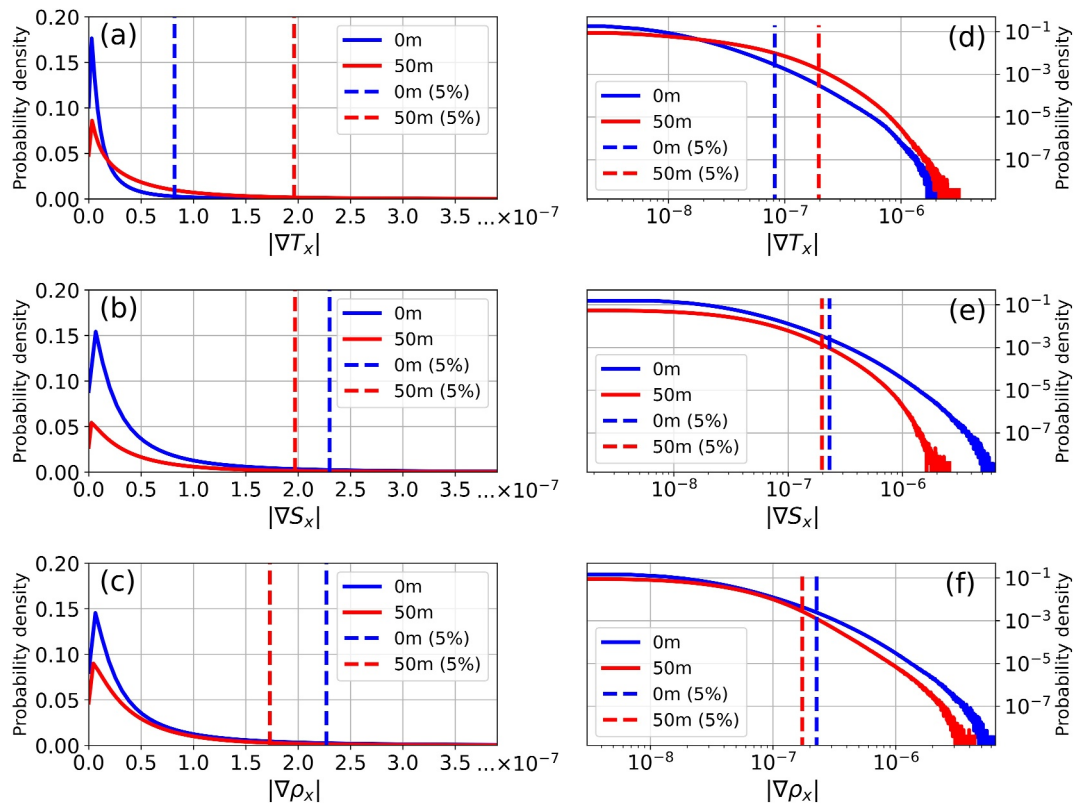


Figure 7. Probability density function (PDF) for (a) $|\nabla T_x|$, (b) $|\nabla S_x|$ and (c) $|\nabla \rho_x|$ in the BoB, denoted by solid lines (blue for 0 m and red for 50 m). Dashed lines represent the top 5% magnitude of each gradient (d–f) are the corresponding PDF in logarithmic scale.

$|\nabla T_x|$ threshold is about three times smaller than those of $|\nabla S_x|$ and $|\nabla \rho_x|$, while at the subsurface (red lines in Figure 7), the $|\nabla T_x|$ threshold is nearly identical to that of $|\nabla S_x|$ and larger than that of $|\nabla \rho_x|$. Meanwhile, the magnitudes of top 5% of surface $|\nabla S_x|$ and $|\nabla \rho_x|$ are larger than at subsurface, while the top 5% of $|\nabla T_x|$ at subsurface are larger than at surface in logarithmic scale (Figures 7d~7f).

5. Compensated and Reinforced Fronts in the nBoB

5.1. Quantify the Role of Compensation/Reinforcement

The density ratio (R_x) and Turner angle (Tu_x) are widely used to quantify the compensation/reinforcement effects (Ferrari & Rudnick, 2000). They are calculated by:

$$R_x = -\nabla T_x / \nabla S_x \quad (4.1)$$

$$Tu_x = \arctan R_x \quad (4.2)$$

where the negative sign means that the density decreases with temperature but increases with salinity. Since R_x can be very small (large) due to very small ∇T_x (∇S_x), it is more convenient to use Tu_x within a finite range ($-\pi/2 < Tu_x < \pi/2$), as was done by Spiro Jaeger and Mahadevan (2018) and Drushka et al. (2019).

A snapshot of Tu_x on 29 April 2012 in region R1 is shown in Figure 8a. Positive and negative Tu_x appear alternately in the nBoB, indicating the roles of compensation and reinforcement, respectively. Here, we classified the fronts into four types according to the value of Tu_x : Temperature Controlled Salinity Reinforcing (TCSR) with $-\pi/2 < Tu_x \leq -\pi/4$; Salinity Controlled Temperature Reinforcing (SCTR) with $-\pi/4 < Tu_x \leq 0$; Salinity Controlled Temperature Opposing (SCTO) with $0 < Tu_x \leq \pi/4$; Temperature Controlled Salinity Opposing (TCSO) with $\pi/4 < Tu_x < \pi/2$.

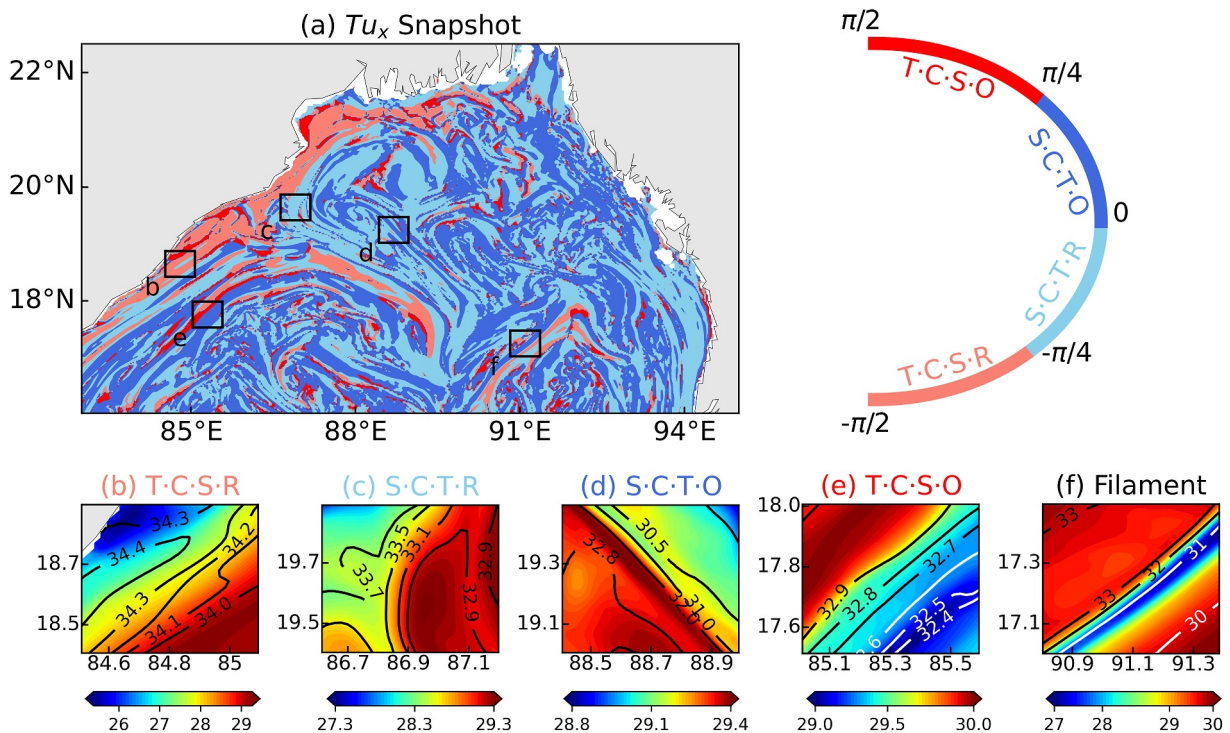


Figure 8. (a) Snapshot of normalized surface Tu_x on 29 April 2012 in region R1 (b–f) are the SST and SSS structure from the black boxes in (a): (b) TCSR front, (c) SCTR front, (d) SCTO front, (e) TCSO front and (f) cold filament. Note that the color shadings in (b–f) are for temperature ($^{\circ}$ C) and the contours are for salinity (PSU).

Several examples of each type of front in terms of horizontal temperature and salinity structure are shown in Figures 8b–8f from the Tu_x snapshot. The TCSR front is featured with warm/fresh water on the southeastern side and cold/salty water on the northwestern side (Figure 8b). The SCTR front is featured with warm/fresh water on the eastern side and cold/salty water on the western side (Figure 8c). The SCTO front is featured with warm/salty water on the southwestern side and cold/fresh water on the northeastern side (Figure 8d). The TCSO front is featured with warm/salty water on the western side and cold/salty water on the eastern side (Figure 8e). Figure 8f shows a special cold filament structure (Gula et al., 2014), which is a combination of SCTO and TCSR fronts. It is featured with cold water lying in the middle of warm water, and salinity increasing northwestward.

5.2. Statistics of Compensated/Reinforced Fronts

Since there is a large discrepancy in horizontal gradients between the coastal (<200 m) and offshore (>200 m) regions, as well as between the surface and subsurface layers (Figure 5), the statistics of Tu_x are analyzed here using the conditional PDF method, and the 5% thresholds are used here to separate the frontal regions (Figure 9). Hereafter we mostly focus on the frontal regions in region R1.

For regions with top 5% of $|\nabla T_x|$ (Figures 9a and 9b), we can first expect that no Tu_x are near zero because of the large values of $|\nabla T_x|$. At the surface (blue lines), there is a peak of Tu_x located in $(0, \pi/4)$ for both coastal and offshore regions as SCTO fronts. In other words, regions with top 5% magnitudes of $|\nabla T_x|$ are featured with even larger $|\nabla S_x|$. Apart from the SCTO fronts, the probabilities of the remaining three types of fronts at surface are almost identical. At subsurface (red lines), large $|\nabla T_x|$ are more likely to be fully compensated by $|\nabla S_x|$ with a peak near $\pi/4$, especially far from the coast.

The condition for top 5% of $|\nabla S_x|$ are quite different from that of $|\nabla T_x|$ in terms of the conditional PDF of Tu_x (Figures 9c and 9d). No values of Tu_x are near $\pm\pi/2$ for large $|\nabla S_x|$. Almost all the values of Tu_x are concentrated at $(-\pi/4, \pi/4)$, showing the predominance of salinity. The shape of the PDF at surface is characterized by a peak near 0, but there are still more positive (compensation) Tu_x than negative (reinforcement) ones. At subsurface, the peak of Tu_x is close to $\pi/4$, which is similar to the subsurface $|\nabla T_x|$, suggesting the tendency to be fully compensated.

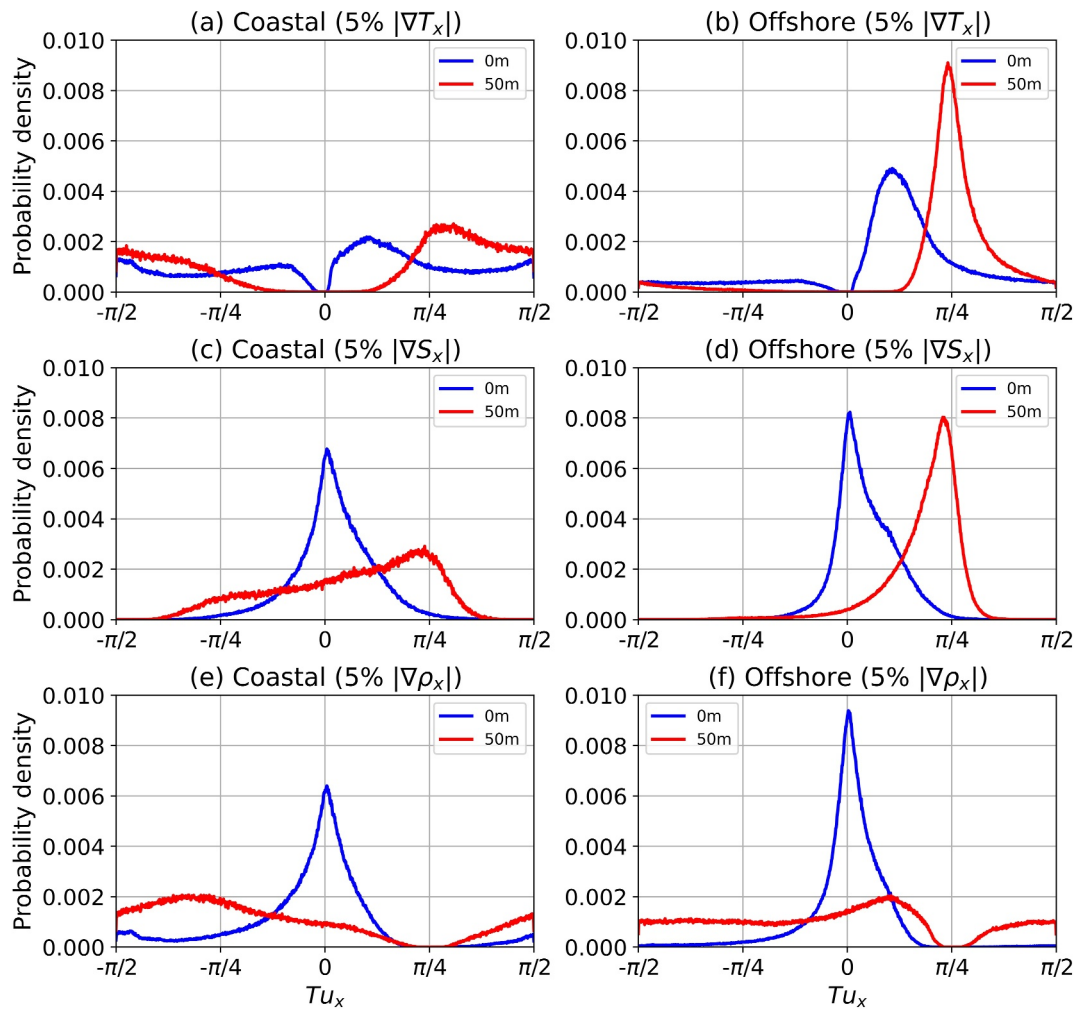


Figure 9. Conditional PDF of Tu_x at (a) coastal regions with top 5% of $|\nabla T_x|$, (b) offshore regions with top 5% of $|\nabla T_x|$, (c) coastal regions with top 5% of $|\nabla S_x|$, (d) offshore regions with top 5% of $|\nabla S_x|$, (e) coastal regions with top 5% of $|\nabla \rho_x|$ and (f) offshore regions with top 5% of $|\nabla \rho_x|$. Blue lines for surface Tu_x and red lines for subsurface Tu_x .

The shape of the Tu_x PDF for the top 5% of $|\nabla \rho_x|$ at surface is similar to that of $|\nabla S_x|$ (Figures 9e and 9f). It is not possible for density fronts to be fully compensated, so no values of Tu_x are near $\pi/4$. At subsurface, there are more negative Tu_x (reinforcement effect) distributed over the coastal region, and this can help explain the large values of coastal $|\nabla \rho_x|$ in Figure 5f.

5.3. Seasonality of Compensated Fronts Versus Reinforced Fronts

According to the frontal classification method, we can further evaluate the seasonal variation of compensated fronts versus reinforced fronts over the study region. The ratios of compensation (dark colors) and reinforcement (light colors) effects for the top 5% of $|\nabla T_x|$, $|\nabla S_x|$ and $|\nabla \rho_x|$ during different seasons are shown in Figure 10. Overall, the seasonal variations are more pronounced at surface than at subsurface, considering that the surface layer is directly influenced by the seasonal atmospheric fluxes. Surface compensation is most likely to occur during winter, especially for $|\nabla T_x|$ and $|\nabla S_x|$ (more than 80%). The fresher side of a front is characterized by shallow MLD, so the temperature on this side will decrease more than on the saltier side when the ocean surface loses heat. As a result, there will be colder/fresher water on the one side and warmer/saltier water on the other side, and they will be compensated. This cooling-induced compensation has been revealed by Spiro Jaeger and Mahadevan (2018) and is further validated here.

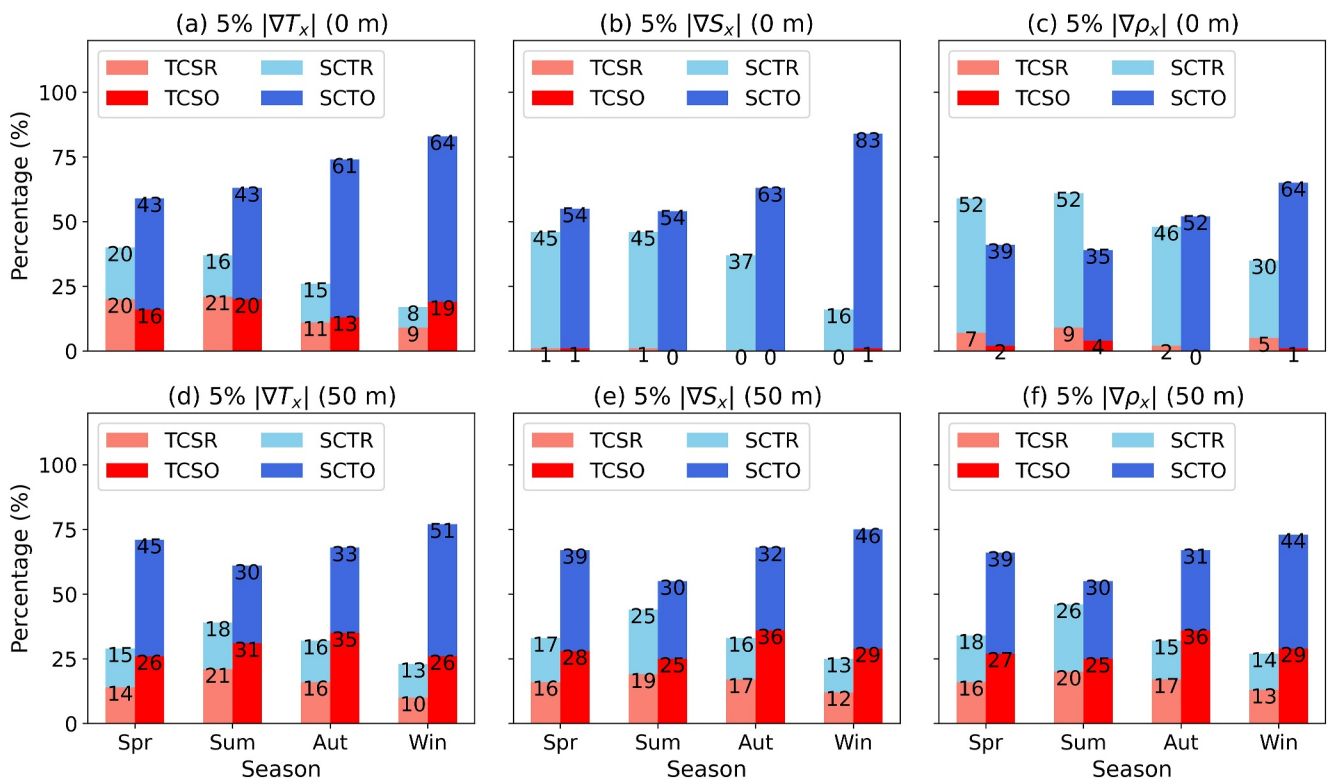


Figure 10. Seasonal ratio (%) of compensated (dark color bars) and reinforced fronts (light S color bars) in region R1 for (a) surface top 5% of $|\nabla T_x|$, (b) surface top 5% of $|\nabla S_x|$, (c) surface top 5% of $|\nabla \rho_x|$ (d–f) are the same as (a–c) but for subsurface.

At the subsurface, the compensation ratio is also largest in winter, indicating the penetration of cooling-induced compensation to the subsurface. However, the effects of atmospheric flux are apparently reduced in terms of its weaker seasonal variation at subsurface. Moreover, the dominance of compensation over reinforcement at subsurface is present during all seasons. In spring, when the ocean is heated, the surface fronts are less compensated, while the subsurface fronts are almost as compensated as in winter. This enhanced subsurface compensation cannot be explained by the cooling-induced effect. Other factors must be responsible for this phenomenon. In the next subsection, we will briefly explain the subsurface spring compensation.

5.4. Scale-Dependent Compensation

The aforementioned compensation effect is actually composed of different spatial scales of compensation. The submesoscale-selective compensation has been revealed in the BoB (Spiro Jaeger & Mahadevan, 2018) and Taiwan Strait (Lin et al., 2023) by using ship-based observations, respectively. Here, we attempt to validate whether this submesoscale-selective character is robust in the model data.

By choosing different horizontal sampling intervals from the model data, we can calculate the tracer gradients at different scales, and compare the results with the model grid scale of ~ 4 km (central difference, so 2 times of grid space). The time-depth compensation ratio for ~ 4 km and ~ 100 km scales are shown in Figures 11a and 11b. Here the compensation ratio is defined as the ratio of the compensated grids over total grids for each day at each depth. In general, the compensation effect is weaker at larger scales. Strong compensation signals ($>70\%$) almost disappear at ~ 100 km at subsurface, suggesting that the compensation effect at subsurface is submesoscale-selective.

The compensation effects at surface and subsurface have some similarities. As the surface layer is better mixed by atmospheric turbulence, the surface compensation ratio is in general smaller than that of subsurface (Figure 11c). The expected subsurface compensation ratio (surface value adds 8%, blue dashed line in Figure 11c) agrees well with the real value (blue solid line in Figure 11c), except during spring/early summer when it is featured with a rapid shallowing of mixed layer depth. While the surface compensation during spring/early summer is much

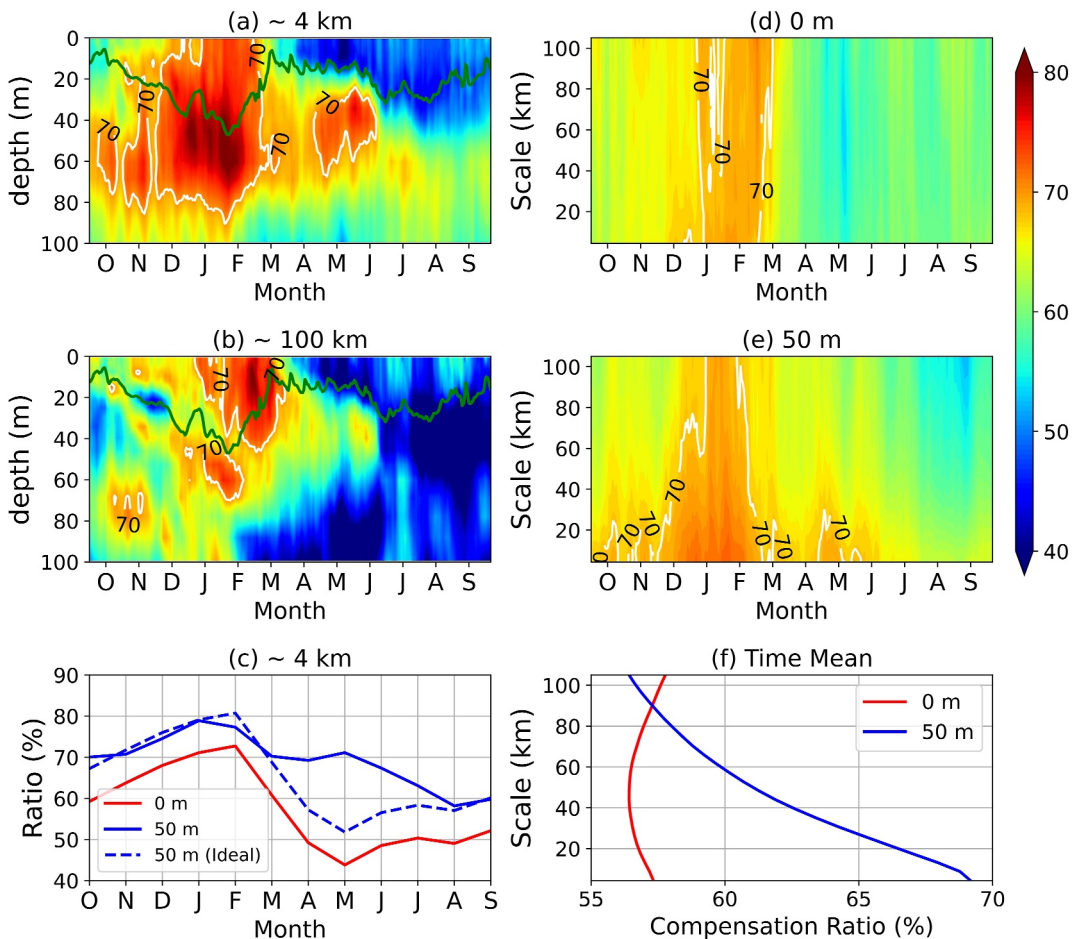


Figure 11. Time-depth plots of ratio (%) of compensation in region R1 for spatial scales of (a) ~ 4 km and (b) ~ 100 km. (c) Monthly mean and regional mean time series of compensation ratio at 0 m (red solid line), 50 m (blue solid line) and expected value at 50 m (blue dashed line) for model grid scale. Compensation ratio as a function of scale and time at (d) 0 m depth and (e) 50 m depth. (f) Annual mean compensation ratio for different scales at 0 m (red line) and 50 m (blue line). Green lines in (a) and (b) show the mixed layer depth. White contours in (a, b, d and e) show the 70% compensation ratio.

reduced by surface warming, large value of subsurface compensation still holds because of the blocking effects of the mixed layer base.

A more accurate analysis between compensation ratio and sample interval is done, and the compensation at subsurface is shown to be very sensitive to the spatial scale all the time (Figure 11e). During autumn and spring, for example, the grid scale (~ 4 km) compensation is quite obvious at subsurface, but it gets weaker quickly toward scales larger than $20 \sim 40$ km. In comparison, at surface the phenomenon that compensation rapidly diminishes toward larger scales only occurs during early winter (Figure 11d), which is the period of the observational data in Spiro Jaeger and Mahadevan (2018). Large discrepancies of scale dependency of compensation are visible from the annual mean compensation ratios at surface and subsurface (Figure 11f). It is suggesting that a more detailed observation with a longer time span is needed to verify the robustness of submesoscale-selective compensation at surface.

6. Stratification Induced by Compensated Fronts

6.1. Statistical Relation

As mentioned in Section 3, the barrier layer is thick in winter and thin in spring (Figure 2), together with the occurrence of subsurface temperature inversion in winter. Compensated fronts also prevail during winter, as seen in Section 5. Atmospheric cooling seems to play a dominant role, but oceanic processes are also significant. To

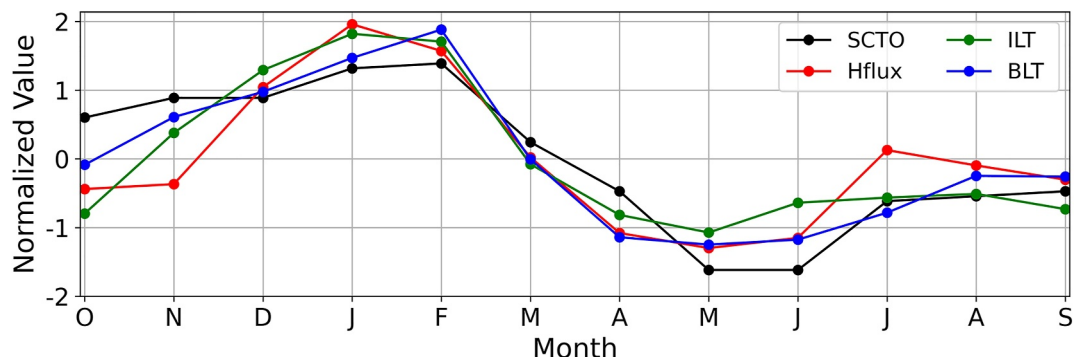


Figure 12. Time series of ratio of SCTO (black), regional average heat flux (red), ILT (green) and BLT (blue) over region R1. All values are normalized by their mean values and standard deviations.

illustrate the statistical relationship between atmospheric forcing, oceanic fronts and vertical stratification, several variables are selected for comparison: (a) ratio of compensation; (b) regional mean barrier layer thickness (BLT); (c) regional mean temperature inversion layer thickness (ILT, defined as the layer where the vertical temperature gradient is negative); and (d) regional mean heat flux.

Here the surface, SCTO, density fronts are chosen as a representation of the compensation ratio for several seasons. First, SCTO fronts are much more popular over the nBoB region than TCSO fronts. Second, the density fronts are more appropriate than salinity/temperature fronts, as density is directly related to the pressure gradients and thus ocean movement. Last but not least, surface fronts are characterized by more obvious seasonal variations than subsurface fronts.

The mutual correlation between all variables is quite good, all peaks in winter and troughs in late spring/summer (Figure 12). The ocean loses heat during winter and gains heat during late spring and summer. Under the condition of horizontal salinity gradients, compensated fronts are most prominent in winter due to the cooling-induced compensation effect. Meanwhile, the cooling effect forms a deeper thermocline than the halocline and creates a thick barrier layer. The barrier layer can limit the winter cooling to the shallow surface layer, and warm water can be trapped in the subsurface layer, creating a temperature inversion.

Numerical studies have shown that temperature inversions can also form when the compensated fronts collapse (Pham and Sarkar et al., 2019; Ramachandran & Tandon, 2020; Spiro Jaeger & Mahadevan, 2018). Thus, in addition to the atmospheric cooling effect, oceanic frontal dynamics may also be responsible for the vertical stratification in frontal regions. Considering that there are four types of fronts (TCSR, SCTR, SCTO and TCSO), the resulting stratification may be quite different for different fronts. To illustrate the specific frontal processes for different fronts, idealized frontal experiments are conducted in the next section.

6.2. Idealized Numerical Model

In this subsection, four sets of frontal experiments with different types of fronts using CROCO are conducted, and the model setups are described in Section 2. The models are run for 2.5 days, and the initial state and final states are selected for comparison.

Regardless of the frontal type, the isopycnals are tilted (third column in Figure 13), so the fronts will slump due to the gravitational effect. The frontal types are indicated by the initial values of Tu_x (fourth column in Figure 13). The values of the Turner angle in the vertical direction (Tu_z) are also shown (last column in Figure 13). Tu_z is calculated by:

$$Tu_z = \arctan(-\nabla T_z / \nabla S_z) \quad (5)$$

It represents the effects of vertical compensation/reinforcement. In the initial state, the warm/fresh water is in the surface and the cold/salty water is in the subsurface, so Tu_z is negative everywhere (reinforcement).

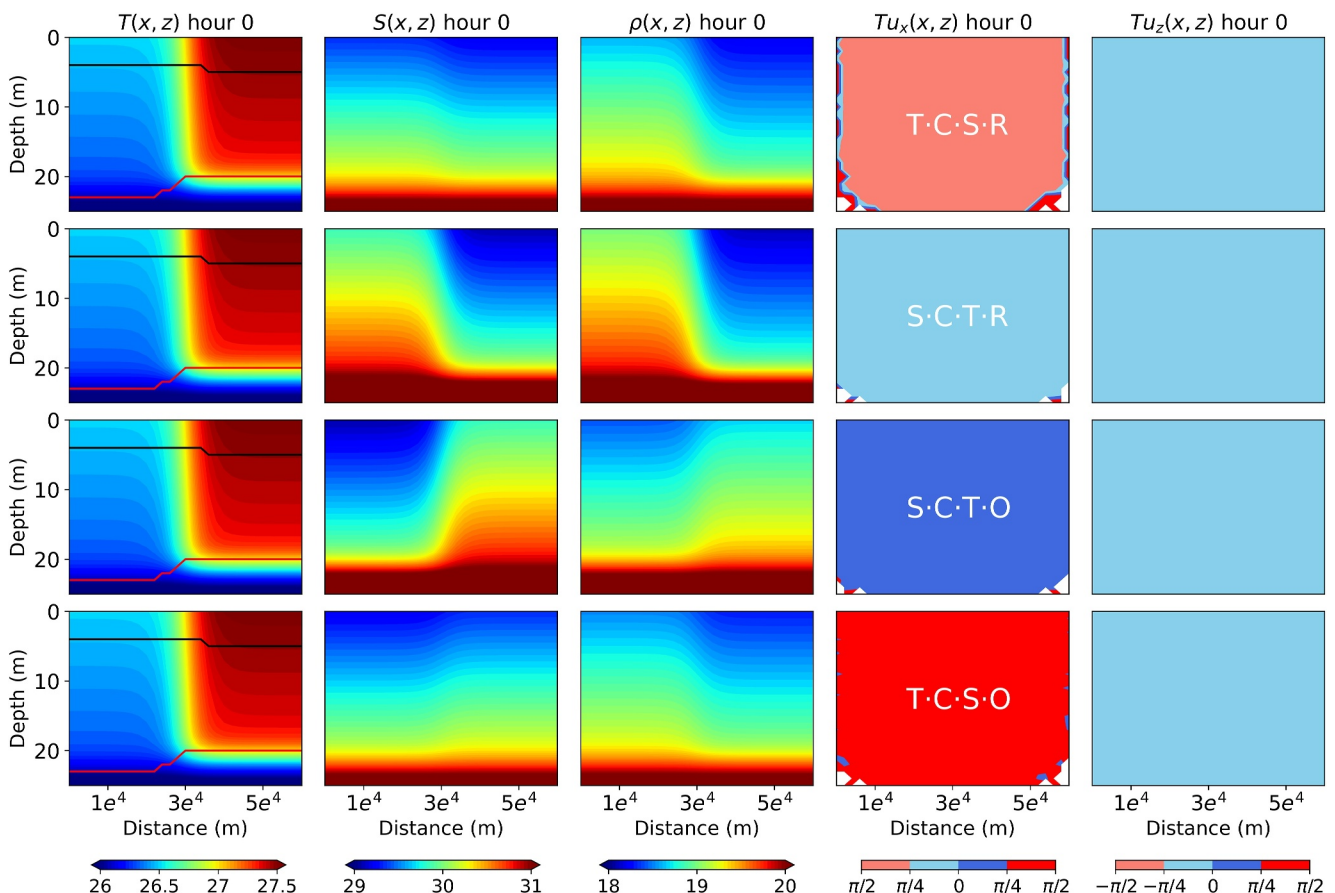


Figure 13. The cross front temperature (first column), salinity (second column), density (third column), Tu_x (fourth column) and Tu_z (last column) for TCSR front (first row), SCTR front (second row), SCTO front (third row), and TCSO front (last row) of the initial state. Black lines represent the MLD and red lines represent the ILD. The layer in between is the barrier layer.

The final state after 2.5 days of running is shown in Figure 14. As the lighter waters are located on the right side of TCSR, SCTR and TCSO fronts (third column in Figure 13), they all tend to slump to the left, and the warm water tends to overlay the cold water (first column in Figure 14). Temperature inversion does not occur and the BLTs are reduced more or less by the slump of the isotherms. The values of Tu_z remain negative for these three fronts (last column in Figure 14).

The evolution of the SCTO front is quite different from other fronts (third row in Figure 14). In this case, the lighter waters are on the left side of the front. When the front slumps, the fresh waters tend to be above the salty waters, but the warm waters tend to be below the cold waters due to the tilt of the isotherms. Also, the ILD remains deep, so the barrier layer remains thick. The values of Tu_z become positive around the temperature inversion region, indicating the vertical compensation effect. These results may help to further explain why SCTO fronts and temperature inversion layers/barrier layer are collocated.

7. Discussion and Conclusions

In this study, we used high-resolution model output (LLC4320) to investigate the characteristics of compensated/reinforced submesoscale fronts in the northern BoB. The model is shown to describe the main temperature and salinity features in the study region realistically. Large surface horizontal temperature, salinity and density gradients occur over the northern bay, with salinity/density gradients nearly 3 times larger than temperature gradients. At subsurface, temperature gradients are apparently increased compared to that at surface, while density gradients are much reduced due to the increasing counteracting effect between temperature and salinity.

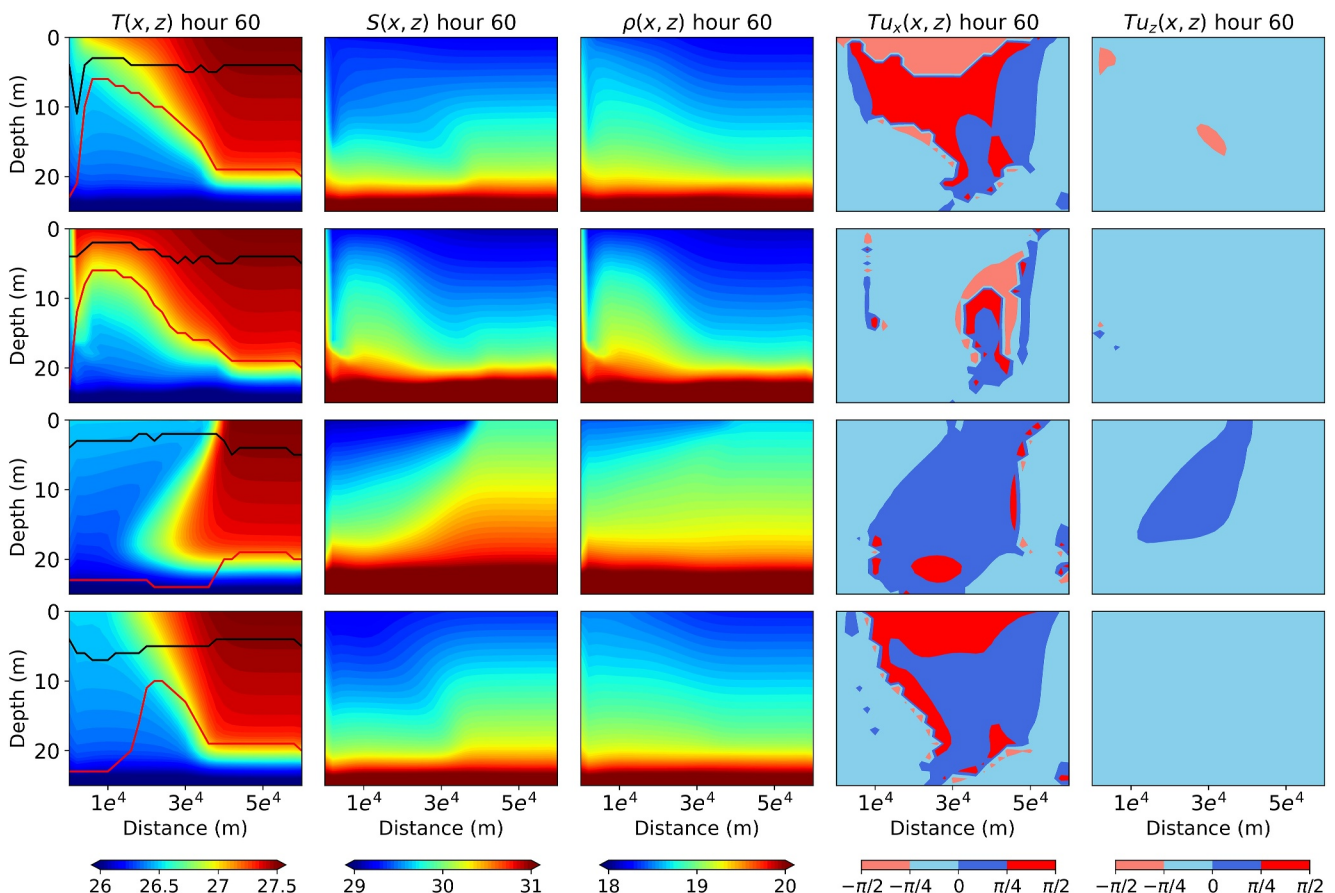


Figure 14. The same as Figure 13, but after 2.5 days of model running.

Probability density functions of gradients tend to flatten at magnitudes of the largest 5% of each gradient, and regions where gradients larger than these thresholds are considered as submesoscale frontal regions. The roles of compensation and reinforcement across fronts are quantified using the Turner angle. Based on the value of the Turner angle, submesoscale fronts are classified into 4 types: SCTO (salinity-controlled fronts compensated by temperature), SCTR (salinity-controlled fronts reinforced by temperature), TCSO (temperature-controlled fronts compensated by salinity), and TCSR (temperature-controlled fronts reinforced by salinity).

The statistics of different types of fronts are analyzed. Surface fronts are mostly controlled by salinity and partly compensated by temperature, while subsurface fronts are controlled by both temperature and salinity and tend to be fully compensated. Seasonal variations for surface fronts are more pronounced than for subsurface fronts, with SCTO fronts being most pronounced in winter, due to the combined effects of the existence of strong salinity fronts and heat losses of the ocean. The subsurface layer features with more compensation than the surface layer, and the submesoscale-selective compensation is proved to be more evident at subsurface by choosing different horizontal sampling intervals. The SCTO fronts are suggested to be closely related to the vertical barrier layer and temperature inversion, and this is further confirmed by idealized models. The intermittent appearance of the temperature inversion layer and the barrier layer in the BoB region may be related to the formation and dissolution of compensated submesoscale fronts.

The subsurface compensation is shown to be an inherent feature in the ocean. When the idealized fronts (Section 6) slumps, a lot of compensation signals occur at subsurface (5–15 m in this case) for different types of fronts. Zonal sections of Tu_x and Tu_z from LLC4320 for a typical spring day are shown in Figure 15. Positive Tu_x are mostly confined at subsurface (compensation), while negative Tu_z are dominated below the mixed layer in order to stay vertical stable. At subsurface, Tu_z is combined with positive values (compensation) and small negative values (weak reinforcement). Under a small disturbance, the vertical weak reinforcement is easy to change its sign

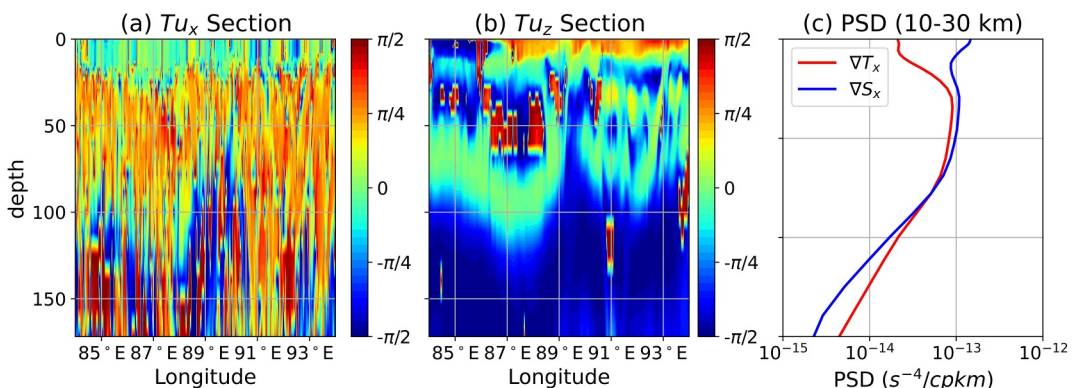


Figure 15. Zonal section of (a) Tu_x and (b) Tu_z from LLC4320 for a typical spring day. (c) Annual mean and regional averaged power spectrum density (PSD) of ∇T_x and ∇S_x at submesoscale range (10–30 km) in logarithmic scale.

to compensation, and the vertical compensation can easily convert to horizontal compensation when the isopycnals tilt. At surface, although large vertical compensation exists, the surface wind stirs and homogenizes this layer, so compensation is less prevailing. This subsurface layer is the so called pycnocline by Spiro Jaeger et al. (2020), which is featured with most remarkable spice variation, and can be proved from the submesoscale (10–30 km) power spectrum density (PSD) for ∇T_x and ∇S_x (Figure 15c). This can help to explain why subsurface compensation is much more pronounced and more submesoscale-selective than surface.

A front is either compensated or reinforced. Compensated fronts are characterized with a density gradient at least smaller than either temperature gradient or salinity gradient, while reinforced fronts are featured with larger density gradient than both temperature and salinity gradient. Compensated fronts with smaller density gradients are thus not favorable for frontal instability and associated energy transfer and transformation compared to reinforced fronts. In an ideal ocean without any forcing, temperature and salinity always tend to be fully compensated in order to get a completely stable state. But in the real ocean, this is never the truth thanks to the omnipresent disturbance.

There are still some limitations of the model data. For example, the temporal frequency and the way to include river run-off in the model may impact the submesoscale fronts, especially the coastal regions close to the river mouth. The model is using climatological river discharge and converting it to freshwater flux, and the season variation of river discharge is not included. As a result, the model overestimates freshwater in spring and underestimates freshwater in autumn. Additionally, converting river freshwater into surface flux may omit the river diffusion processes, which could generate some small scale processes. The submesoscale salinity fronts captured by the model may be underestimated. A real river forcing with relative high frequency is needed to better understand the submesoscale frontal dynamics around the river mouth.

Data Availability Statement

The authors declare that the data supporting the findings of this study are available within the article and the multisource data used in this study can all be found online. The LLC4320 model output used for analysis can be directly accessed from the ECCO Data Portal via https://data.nas.nasa.gov/ecco/eccodata/lc_4320/ (Menemenlis et al., 2008). The WOA18 climatological temperature and salinity data used for model validation are available at <https://www.ncei.noaa.gov/products/world-ocean-atlas> (Locarnini et al., 2018; Zweng et al., 2018). Sea surface salinity data from SMOS L4 used for model validation are available at https://data.catds.fr/cecos-locean/Ocean_products/SSS_SMOS-SMAP_OI_L4/ (Kolodziejczyk et al., 2021). Sea surface temperature from GRSST used for model validation can be downloaded from <https://www.ncei.noaa.gov/data/oceans/ghrsst/L4/> (Dash et al., 2012). MODIS L3 satellites observed sea surface temperature data are available at <https://oceancolor.gsfc.nasa.gov/l3/> (Savtchenko et al., 2004). The idealized CROCO model (Auclair et al., 2022) outputs for different types of fronts are available at <https://doi.org/10.5281/zenodo.1323543>. Figures were made with Matplotlib version 3.9.0 at <https://doi.org/10.5281/zenodo.11201097> and available under the Matplotlib license at <https://matplotlib.org/> (Hunter, 2007).

Acknowledgments

This study was supported by the National Natural Science Foundation of China (42276014, 42276189, 41876002), Science and Technology Planning Project of Guangdong Province, China (Grant number 2022B1212050003), and supported by High Performance Computing Platform, Hohai University.

References

- Arbic, B. K., Eliot, S., Brasch, J. M., Menemenlis, D., Ponte, A. L., Shriver, J. F., et al. (2022). Near-surface oceanic kinetic energy distributions from drifter observations and numerical models. *Journal of Geophysical Research: Oceans*, 127(10), e2022JC018551. <https://doi.org/10.1029/2022JC018551>
- Auclair, F., Benshila, R., Bordois, L., Boutet, M., Brémond, M., Caillaud, M., et al. (2022). Coastal and regional ocean community model. *Zenodo*. <https://doi.org/10.5281/zenodo.7415055>
- Balwada, D., Xie, J. H., Marino, R., & Feraco, F. (2022). Direct observational evidence of an oceanic dual kinetic energy cascade and its seasonality. *Science Advances*, 8(41), eabq2566. <https://doi.org/10.1126/sciadv.abq2566>
- Barkan, R., McWilliams, J. C., Molemaker, M. J., Choi, J., Srinivasan, K., Schepetkin, A. F., & Bracco, A. (2017). Submesoscale dynamics in the northern Gulf of Mexico. Part II: Temperature–salinity relations and cross-shelf transport processes. *Journal of Physical Oceanography*, 47(9), 2347–2360. <https://doi.org/10.1175/JPO-D-17-0040.1>
- Barkan, R., Molemaker, M. J., Srinivasan, K., McWilliams, J. C., & D’Asaro, E. A. (2019). The role of horizontal divergence in submesoscale frontogenesis. *Journal of Physical Oceanography*, 49(6), 1593–1618. <https://doi.org/10.1175/JPO-D-18-0162.1>
- Barkan, R., Srinivasan, K., Yang, L., McWilliams, J. C., Gula, J., & Vic, C. (2021). Oceanic mesoscale eddy depletion catalyzed by internal waves. *Geophysical Research Letters*, 48(18), e2021GL094376. <https://doi.org/10.1029/2021GL094376>
- Boccaletti, G., Ferrari, R., & Fox-Kemper, B. (2007). Mixed layer instabilities and restratification. *Journal of Physical Oceanography*, 37(9), 2228–2250. <https://doi.org/10.1175/JPO3101.1>
- Cheng, X., Li, L., Jing, Z., Cao, H., Zhou, G., Duan, W., & Zhou, Y. (2023). Seasonal features and potential mechanisms of submesoscale processes in the southern Bay of Bengal during 2011/12. *Journal of Physical Oceanography*, 53(4), 1199–1217. <https://doi.org/10.1175/JPO-D-22-0078.1>
- Clayton, S., Nagai, T., & Follows, M. J. (2014). Fine scale phytoplankton community structure across the Kuroshio Front. *Journal of Plankton Research*, 36(4), 1017–1030. <https://doi.org/10.1093/plankt/fbu020>
- Dash, P., Ignatov, A., Martin, M., Donlon, C., Brasnett, B., Reynolds, R. W., et al. (2012). Group for high resolution SST (GHRSST) analysis fields inter-comparisons part 2. Near real-time web-based level 4 SST quality monitor (L4-SQUAM). *Deep Sea Research Part II: Topical Studies in Oceanography*, 77, 31–43. <https://doi.org/10.1016/j.dsr2.2012.04.002>
- De Boyer Montégut, C., Madec, G., Fischer, A. S., Lazar, A., & Iudicone, D. (2004). Mixed layer depth over the global ocean: An examination of profile data and a profile-based climatology. *Journal of Geophysical Research*, 109(C12). <https://doi.org/10.1029/2004jc002378>
- Dong, J., Fox-Kemper, B., Zhang, H., & Dong, C. (2020). The scale of submesoscale baroclinic instability globally. *Journal of Physical Oceanography*, 50(9), 2649–2667. <https://doi.org/10.1175/JPO-D-20-0043.1>
- Dong, J., Fox-Kemper, B., Zhang, H., & Dong, C. (2021). The scale and activity of symmetric instability estimated from a global submesoscale-permitting ocean model. *Journal of Physical Oceanography*, 51(5), 1655–1670. <https://doi.org/10.1175/JPO-D-20-0159.1>
- Drushka, K., Asher, W. E., Sprintall, J., Gille, S. T., & Hoang, C. (2019). Global patterns of submesoscale surface salinity variability. *Journal of Physical Oceanography*, 49(7), 1669–1685. <https://doi.org/10.1175/JPO-D-19-0018.1>
- Ferrari, R., & Rudnick, D. L. (2000). Thermohaline variability in the upper ocean. *Journal of Geophysical Research*, 105(C7), 16857–16883. <https://doi.org/10.1029/2000JC900057>
- Garabato, A. C. N., Yu, X., Callies, J., Barkan, R., Polzin, K. L., Frajka-Williams, E. E., et al. (2022). Kinetic energy transfers between mesoscale and submesoscale motions in the open ocean’s upper layers. *Journal of Physical Oceanography*, 52(1), 75–97. <https://doi.org/10.1175/JPO-D-21-0099.1>
- Gula, J., Molemaker, M. J., & McWilliams, J. C. (2014). Submesoscale cold filaments in the Gulf Stream. *Journal of Physical Oceanography*, 44(10), 2617–2643. <https://doi.org/10.1175/JPO-D-14-0029.1>
- Hoskins, B. J., & Bretherton, F. P. (1972). Atmospheric frontogenesis models: Mathematical formulation and solution. *Journal of the Atmospheric Sciences*, 29(1), 11–37. [https://doi.org/10.1175/1520-0469\(1972\)029<0011:AFMMFA>2.0.CO;2](https://doi.org/10.1175/1520-0469(1972)029<0011:AFMMFA>2.0.CO;2)
- Hunter, J. D. (2007). Matplotlib: A 2d graphics environment. *Computing in Science and Engineering*, 9(3), 90–95. <https://doi.org/10.1109/MCSE.2007.551>
- Jensen, T. G., Shulman, I., Wijesekera, H. W., Anderson, S., & Ladner, S. (2018). Submesoscale features and their interaction with fronts and internal tides in a high-resolution coupled atmosphere-ocean-wave model of the Bay of Bengal. *Ocean Dynamics*, 68(3), 391–410. <https://doi.org/10.1007/s10236-018-1136-x>
- Kolodziejczyk, N., Hamon, M., Boutin, J., Vergely, J. L., Reverdin, G., Supply, A., & Reul, N. (2021). Objective analysis of SMOS and SMAP sea surface salinity to reduce large-scale and time-dependent biases from low to high latitudes. *Journal of Atmospheric and Oceanic Technology*, 38(3), 405–421. <https://doi.org/10.1175/JTECH-D-20-0093.1>
- Lévy, M., Franks, P. J. S., & Smith, K. S. (2018). The role of submesoscale currents in structuring marine ecosystems. *Nature Communications*, 9(1), 4758. <https://doi.org/10.1038/s41467-018-07059-3>
- Li, L., Cheng, X., Jing, Z., Cao, H., & Feng, T. (2022). Submesoscale motions and their seasonality in the northern Bay of Bengal. *Acta Oceanologica Sinica*, 41(4), 1–13. <https://doi.org/10.1007/s13131-021-1847-6>
- Lin, H., Xu, S., Liu, Z., Hu, J., Zhang, F., & Cao, Z. (2023). Scale-dependent temperature–salinity compensation in frontal regions of the Taiwan Strait. *Journal of Geophysical Research: Oceans*, 128(2), e2022JC019134. <https://doi.org/10.1029/2022JC019134>
- Locarnini, R. A., Mishonov, A. V., Baranova, O. K., Boyer, T. P., Zweng, M. M., Garcia, H. E., et al. (2018). *World Ocean Atlas 2018, volume 1: Temperature*. A. Mishonov technical ed (Vol. 81, p. 52pp). NOAA Atlas NESDIS.
- Lukas, R., & Lindstrom, E. (1991). The mixed layer of the western equatorial Pacific Ocean. *Journal of Geophysical Research*, 96(S01), 3343–3357. <https://doi.org/10.1029/90JC01951>
- MacKinnon, J. A., Nash, J. D., Alford, M. H., Lucas, A., Mickett, J., Shroyer, E., et al. (2016). A tale of two spicy seas. *Oceanography*, 29(2), 50–61. <https://doi.org/10.5670/oceanog.2016.38>
- Mahadevan, A. (2016). The impact of submesoscale physics on primary productivity of plankton. *Annual Review of Marine Science*, 8(1), 161–184. <https://doi.org/10.1146/annurev-marine-010814-015912>
- McKie, T., Lucas, A. J., & MacKinnon, J. (2024). Submesoscale dynamics in the Bay of Bengal: Inversions and instabilities. *Journal of Geophysical Research: Oceans*, 129(3), e2023JC020563. <https://doi.org/10.1029/2023JC020563>
- McWilliams, J. C. (2016). Submesoscale currents in the ocean. *Proceedings of the Royal Society A: Mathematical, Physical and Engineering Sciences*, 472(2189), 20160117. <https://doi.org/10.1098/rspa.2016.0117>
- McWilliams, J. C. (2021). Oceanic frontogenesis. *Annual Review of Marine Science*, 13(1), 227–253. <https://doi.org/10.1146/annurev-marine-032320-120725>

- McWilliams, J. C., Gula, J., Molemaker, M. J., Renault, L., & Shchepetkin, A. F. (2015). Filament frontogenesis by boundary layer turbulence. *Journal of Physical Oceanography*, 45(8), 1988–2005. <https://doi.org/10.1175/JPO-D-14-0211.1>
- Menemenlis, D., Campin, J. M., Heimbach, P., Hill, C., Lee, T., Nguyen, A., et al. (2008). ECCO2: High resolution global ocean and sea ice data synthesis. *Mercator Ocean Quarterly Newsletter*, 31(October), 13–21.
- Papa, F., Bala, S. K., Pandey, R. K., Durand, F., Gopalakrishna, V. V., Rahman, A., & Rossow, W. B. (2012). Ganga-Brahmaputra river discharge from Jason-2 radar altimetry: An update to the long-term satellite-derived estimates of continental freshwater forcing flux into the Bay of Bengal. *Journal of Geophysical Research*, 117(C11), C11021. <https://doi.org/10.1029/2012jc008158>
- Pham, H. T., & Sarkar, S. (2019). The role of turbulence in strong submesoscale fronts of the Bay of Bengal. *Deep Sea Research Part II: Topical Studies in Oceanography*, 168, 104644. <https://doi.org/10.1016/j.dsrr.2019.104644>
- Poje, A. C., Ozgokmen, T. M., Lipphardt, B. L., Haus, B. K., Ryan, E. H., Haza, A. C., et al. (2014). Submesoscale dispersion in the vicinity of the Deepwater horizon spill. *Proceedings of the National Academy of Sciences*, 111(35), 12693–12698. <https://doi.org/10.1073/pnas.1402452111>
- Ramachandran, S., & Tandon, A. (2020). Generation of submesoscale temperature inversions below salinity fronts in the Bay of Bengal. *Journal of Geophysical Research: Oceans*, 125(12), e2020JC016278. <https://doi.org/10.1029/2020JC016278>
- Ramachandran, S., Tandon, A., Mackinnon, J., Lucas, A. J., Pinkel, R., Waterhouse, A. F., et al. (2018). Submesoscale processes at shallow salinity fronts in the Bay of Bengal: Observations during the winter monsoon. *Journal of Physical Oceanography*, 48(3), 479–509. <https://doi.org/10.1175/JPO-D-16-0283.1>
- Rocha, C. B., Gille, S. T., Chereskin, T. K., & Menemenlis, D. (2016). Seasonality of submesoscale dynamics in the Kuroshio extension. *Geophysical Research Letters*, 43(21), 11–304. <https://doi.org/10.1002/2016GL071349>
- Rudnick, D. L., & Ferrari, R. (1999). Compensation of horizontal temperature and salinity gradients in the ocean mixed layer. *Science*, 283(5401), 526–529. <https://doi.org/10.1126/science.283.5401.526>
- Rudnick, D. L., & Martin, J. P. (2002). On the horizontal density ratio in the upper ocean. *Dynamics of Atmospheres and Oceans*, 36(1–3), 3–21. [https://doi.org/10.1016/S0377-0265\(02\)00022-2](https://doi.org/10.1016/S0377-0265(02)00022-2)
- Sarkar, S., Pham, H. T., Ramachandran, S., Nash, J. D., Tandon, A., Buckley, J., et al. (2016). The interplay between submesoscale instabilities and turbulence in the surface layer of the Bay of Bengal. *Oceanography*, 29(2), 146–157. <https://doi.org/10.5670/oceanog.2016.47>
- Savtchenko, A., Ouzounov, D., Ahmad, S., Acker, J., Leptoukh, G., Koziana, J., & Nickless, D. (2004). Terra and Aqua MODIS products available from NASA GES DAAC. *Advances in Space Research*, 34(4), 710–714. <https://doi.org/10.1016/j.asr.2004.03.012>
- Sengupta, D., Bharath Raj, G. N., Ravichandran, M., Sree Lekha, J., & Papa, F. (2016). Near-surface salinity and stratification in the North Bay of Bengal from moored observations. *Geophysical Research Letters*, 43(9), 4448–4456. <https://doi.org/10.1002/2016GL068339>
- Sengupta, D., Bharath Raj, G. N., & Shenoi, S. S. C. (2006). Surface freshwater from Bay of Bengal runoff and Indonesian throughflow in the tropical Indian Ocean. *Geophysical Research Letters*, 33(22), L22609. <https://doi.org/10.1029/2006GL027573>
- Spiro Jaeger, G., MacKinnon, J. A., Lucas, A. J., Shroyer, E., Nash, J., Tandon, A., et al. (2020). How spice is stirred in the Bay of Bengal. *Journal of Physical Oceanography*, 50(9), 2669–2688. <https://doi.org/10.1175/JPO-D-19-0077.1>
- Spiro Jaeger, G., & Mahadevan, A. (2018). Submesoscale-selective compensation of fronts in a salinity-stratified ocean. *Science Advances*, 4(2), e1701504. <https://doi.org/10.1126/sciadv.1701504>
- Sprintall, J., & Tomczak, M. (1992). Evidence of the barrier layer in the surface layer of the tropics. *Journal of Geophysical Research*, 97(C5), 7305–7316. <https://doi.org/10.1029/92JC00407>
- Su, Z., Wang, J., Klein, P., Thompson, A. F., & Menemenlis, D. (2018). Ocean submesoscales as a key component of the global heat budget. *Nature Communications*, 9(1), 775. <https://doi.org/10.1038/s41467-018-02983-w>
- Thadathil, P., Gopalakrishna, V. V., Muraleedharan, P. M., Reddy, G. V., Araligidad, N., & Shenoy, S. (2002). Surface layer temperature inversion in the Bay of Bengal. *Deep Sea Research Part I: Oceanographic Research Papers*, 49(10), 1801–1818. [https://doi.org/10.1016/S0967-0637\(02\)00044-4](https://doi.org/10.1016/S0967-0637(02)00044-4)
- Thadathil, P., Suresh, I., Gautham, S., Prasanna Kumar, S., Lengaigne, M., Rao, R. R., et al. (2016). Surface layer temperature inversion in the Bay of Bengal: Main characteristics and related mechanisms. *Journal of Geophysical Research: Oceans*, 121(8), 5682–5696. <https://doi.org/10.1002/2016JC011674>
- Thomas, L. N., Tandon, A., & Mahadevan, A. (2008). Submesoscale processes and dynamics. *Ocean Modeling in an Eddying Regime*, 177, 17–38. <https://doi.org/10.1029/177gm04>
- Varkey, M. J., Murty, V. S. N., & Suryanarayana, A. (1996). Physical oceanography of the Bay of Bengal and Andaman sea. *Oceanography and Marine Biology*, 34, 1–70.
- Wenegrat, J. O., Thomas, L. N., Sundermeyer, M. A., Taylor, J. R., D'Asaro, E. A., Klymak, J. M., et al. (2020). Enhanced mixing across the gyre boundary at the Gulf Stream front. *Proceedings of the National Academy of Sciences*, 117(30), 17607–17614. <https://doi.org/10.1073/pnas.2005558117>
- Wijesekera, H. W., Shroyer, E., Tandon, A., Ravichandran, M., Sengupta, D., Jinadasa, S. U. P., et al. (2016). ASIRI: An ocean–atmosphere initiative for Bay of Bengal. *Bulletin of the American Meteorological Society*, 97(10), 1859–1884. <https://doi.org/10.1175/BAMS-D-14-00197.1>
- Wunsch, C. (1998). The work done by the wind on the oceanic general circulation. *Journal of Physical Oceanography*, 28(11), 2332–2340. [https://doi.org/10.1175/1520-0485\(1998\)028<2332:TWDBTW>2.0.CO;2](https://doi.org/10.1175/1520-0485(1998)028<2332:TWDBTW>2.0.CO;2)
- Yu, X., Ponte, A. L., Lahaye, N., Caspar-Cohen, Z., & Menemenlis, D. (2021). Geostrophy assessment and momentum balance of the global oceans in a tide-and eddy-resolving model. *Journal of Geophysical Research: Oceans*, 126(10), e2021JC017422. <https://doi.org/10.1029/2021JC017422>
- Zhou, Y., Duan, W., Cao, H., Zhou, G., Cui, R., & Cheng, X. (2024). Seasonality and potential generation mechanisms of submesoscale processes in the northern Bay of Bengal. *Deep Sea Research Part I: Oceanographic Research Papers*, 208, 104318. <https://doi.org/10.1016/j.dsri.2024.104318>
- Zweng, M. M., Reagan, J. R., Seidov, D., Boyer, T. P., Locarnini, R. A., Garcia, H. E., et al. (2018). *World Ocean Atlas 2018, volume 2: Salinity*. A. Mishonov technical ed (Vol. 82, p. 50pp). NOAA Atlas NESDIS.